



Published in final edited form as:

Nat Biomed Eng. 2018 July ; 2(7): 508–521. doi:10.1038/s41551-018-0230-1.

Rational design of silicon structures for optically controlled multiscale biointerfaces

Yuanwen Jiang^{#1,2}, Xiaojian Li^{#3}, Bing Liu^{#4}, Jaeseok Yi^{1,2}, Yin Fang², Fengyuan Shi⁵, Xiang Gao², Edward Sudzilovsky⁶, Ramya Parameswaran⁷, Kelliann Koehler^{1,2}, Vishnu Nair^{1,2}, Jiping Yue⁸, KuangHua Guo³, Yin Fang¹, Hsiu-Ming Tsai⁹, George Freyermuth¹, Raymond C. S. Wong¹⁰, Chien-Min Kao⁹, Chin-Tu Chen⁹, Alan W. Nicholls⁵, Xiaoyang Wu⁸, Gordon M. G. Shepherd³, and Bozhi Tian^{1,2,11}

¹Department of Chemistry, the University of Chicago, Chicago, IL 60637.

²The James Franck Institute, the University of Chicago, Chicago, IL 60637.

³Department of Physiology, Feinberg School of Medicine, Northwestern University, Chicago, IL 60611.

⁴Department of Neurobiology, The University of Chicago, Chicago, Illinois 60637.

⁵The Research Resources Center, University of Illinois at Chicago, Chicago, IL 60607.

⁶Department of Physics, the University of Chicago, Chicago, IL 60637.

⁷The Graduate Program in Biophysical Sciences, the University of Chicago, Chicago, IL 60637.

⁸Ben May Department for Cancer Research, the University of Chicago, Chicago, IL 60637.

⁹Department of Radiology, the University of Chicago, Chicago, IL 60637.

¹⁰University Research Facility in Behavioral and Systems Neuroscience (UBSN), the Hong Kong Polytechnic University, Hung Hom, Kowloon, Hong Kong.

¹¹The Institute for Biophysical Dynamics, Chicago, IL 60637.

These authors contributed equally to this work.

Abstract

Users may view, print, copy, and download text and data-mine the content in such documents, for the purposes of academic research, subject always to the full Conditions of use:http://www.nature.com/authors/editorial_policies/license.html#termsReprints and permissions information is available at www.nature.com/reprints

Correspondence and requests for materials should be addressed to B.T. (btian@uchicago.edu).

Author Contributions Y.J. and B.T. conceived the idea and designed the experiments. Y.J. fabricated the materials/devices with assistance from J.Y., Y.F. and R.C.S.W.; X. L., B. L. and K.H.G. performed the brain slice and *in vivo* studies; X. L. and B. L. built the instrument and developed the software for *in vivo* neurophysiology experiments and analyses. Y.J., X.G., E.S., R.P., J.Y., G.F. and X.W. performed the cell studies; Y.J., J.Y., F.S., K.K., V.N., Y.F., H.-M.T., C.-M.K., C.-T.C., A.W.N. performed the materials and biointerfaces characterizations; Y.J. developed the photo-response analysis matrix and performed the *COMSOL* simulation; Y.J., X.L., B.L., and B.T. wrote the paper, and received comments and edits from all authors; B.T. and G.M.G.S. mentored the research.

Code availability

Custom codes used to analyze the data are available upon reasonable request to the corresponding author.

Competing financial interest The authors declare no competing financial interests.

Data availability

The authors declare that all data supporting the findings of this study are available within the paper and its supplementary information. Other supporting data are available upon request to the corresponding author.

Silicon-based materials have been widely used. However, remotely controlled and interconnect-free silicon configurations have been rarely explored, because of limited fundamental understanding of the complex physicochemical processes that occur at interfaces between silicon and biological materials. Here, we describe rational design principles, guided by biology, for establishing intracellular, intercellular and extracellular silicon-based interfaces, where the silicon and the biological targets have matched properties. We focused on light-induced processes at these interfaces, and developed a set of matrices to quantify and differentiate the capacitive, Faradaic and thermal outputs from about 30 different silicon materials in saline. We show that these interfaces are useful for the light-controlled non-genetic modulation of intracellular calcium dynamics, of cytoskeletal structures and transport, of cellular excitability, of neurotransmitter release from brain slices, and of brain activity in vivo.

Fundamental discoveries of new forms and new properties in materials can lead to new designs of biophysical tools and biomedical devices^{1–15}. For example, dopant modulated and kinked silicon (Si) nanowires allow for intracellular electrical recording from cardiomyocytes with a field-effect-transistor configuration². Bendable integrated circuits, based on Si nanoscale membranes and their seamless interface with a thermal oxide, open the way for long-lived bioelectronic implants for the heart⁶. Although the electrically registered device components have yielded impressive results, remotely controlled and freestanding systems are rarely employed in biointerface studies^{16–23}. This is largely due to our limited understanding of the physicochemical processes at the freestanding material surfaces under physiological conditions. In particular, a quantitative understanding of the light-induced electrical, electrochemical and thermal pathways across multiple length scales, if achieved, would likely promote future biointerface innovations.

Here, we formulate a rational design principle for a series of Si-based freestanding ‘biotronics’ with length scales from nanometer to centimeter, which establish intra-, inter- and extracellular biointerfaces. The organization of the entire paper follows this order (Supplementary Fig. 1). First, we introduce a biology-guided Si-based biomaterial design, which first considers the material structures and mechanics and then the efficient signal transductions at the Si surfaces in saline. Next, we recommend three classes of materials for establishing biointerfaces across different length scales. Finally, we demonstrate the utility of these new devices by showing light-controlled non-genetic modulations of intracellular calcium dynamics, cytoskeleton-based transport and structures, cellular excitability, neurotransmitter release from brain slices, and brain activities in a mouse model.

The principle of biology-guided biointerface design

Si displays many size- and doping-dependent physicochemical processes. To efficiently leverage these processes in the context of biointerfaces, the Si-based materials or devices should be in tight contact (Fig. 1a, **Selection I**) with their biological counterparts. Such tight interfaces can be established by protein-associated tethering and active motions at the organelle level, by dynamic cellular focal adhesions at the single cell and tissue level, and by van der Waals forces at the organ level. To promote these forces, we focus our Si materials on nanowire geometries (at the organelle level)²⁴, membranes with rough surfaces (at the

cell and tissue level)²⁵, and flexible and distributed meshes (at the organ level)¹, where at least one dimension of the material properties can be tuned to promote tight interfaces (Fig. 1b). After the material/device structures are determined, we are next in a position to examine the effects of other orthogonal controls (*e.g.*, size, doping, surface chemistry) to produce the desirable physicochemical processes (Fig. 1a, **Selection II**) at the biointerfaces. These two-step selections, guided by the need to form tight junctions (**Selection I**) and efficient signal transductions (**Selection II**) with the biological targets, would narrow the material options to those that are better suited for the targeted biophysical or biomedical questions.

Selection for material structures

For example, to enable intracellular biointerfaces, we chose Si nanowires since recent studies showed that they can be internalized into mammalian cells through phagocytosis²⁴ and, when inside, form active interfaces with cytoskeletal systems¹⁴. Additionally, to promote light absorption from single nanowire structures²⁶, we deposited nanocrystalline Si shells over a thin, vapor-liquid-solid (VLS) grown Si nanowire backbone (~ 50 nm in diameter) (Fig. 1c, left and upper right). Cross-sectional and side-view TEM images reveal that > 95% of the total volume is nanocrystalline (Fig. 1c, lower right).

To build extracellular interfaces with single cells or small tissues, we can examine planar Si structures with uniformly doped or dopant modulated configurations to identify the effect of doping. In particular, a *p*-type/intrinsic/*n*-type (*p-i-n*) Si diode junction was synthesized by chemical vapor deposition (CVD) of intrinsic and *n*-type Si layers (~ 140 and ~ 190 nm in thickness, respectively) over a *p*-type Si semiconductor-on-insulator (SOI) substrate (*p*-type Si thickness, ~ 2 μm) (Supplementary Fig. 2). Cross-sectional (scanning) transmission electron microscope (TEM) images taken at the interface between the SOI wafer and the as-deposited layers indicate a columnar shell structure with a sharp and oxide-free interface (< 1 nm junction width) (Fig. 1d, left and upper right). While the *p*-type substrate is single crystalline, the *i/n*-layers are nanocrystalline (Fig. 1d, lower right; Supplementary Fig. 2), which is reminiscent of the Si nanostructures used for thin film solar cells. The surface of the nanocrystalline layer is rough, which would promote cellular focal adhesions²⁵. Beyond doping controls, we also prepared metal (*i.e.*, gold, silver, and platinum) nanoparticle-covered Si diode junctions by electroless deposition in order to expand the repertoire of Si-based biointerfaces (Supplementary Figs. 3–5).

Finally, to create a conformal interface with a soft and curvilinear organ, *e.g.*, a mouse brain cortex, we explored a flexible device made of a distributed mesh of Si membrane (~ 2.3 μm in thickness) and a porous polydimethylsiloxane (PDMS) substrate (~ 120 μm in thickness) (Fig. 1e; Supplementary Fig. 6). The holey structures in both Si and PDMS can mitigate the stress accumulated across a large device area (Supplementary Fig. 7) and enhance the device mechanical compliance.

Selection for material functions

Given that cellular physiology can be altered with a ~ pA level ionic current, we next utilized a high-precision electrochemical tool, *i.e.*, a patch-clamp setup, to investigate the

light-induced and biointerface-relevant physicochemical processes (Fig. 1a, **Selection II**; Fig. 2; **Methods**) that originated from the freestanding Si surfaces²⁷. Briefly, we immersed different types of Si materials (*e.g.*, nanocrystalline nanowires, and dopant-modulated, surface-treated and size-tuned nano-membranes, as selected from the first step) into a phosphate-buffered saline solution and positioned glass micropipette electrodes in close proximity to the Si surfaces ($\sim 2 \mu\text{m}$) where ionic flows across the pipette tips were measured in the voltage-clamp mode (Fig. 2a, upper; Supplementary Fig. 8a). Specifically, we delivered light pulses (530 nm light-emitting diode (LED) or 532 nm laser, 10 ms) through a microscope objective to illuminate Si and recorded the ionic current dynamics under different pipette holding potentials (Fig. 2a, lower; **Methods**).

Using pulsed light illuminations, we developed a universal analysis (**Methods**, “**Analysis of the photo-response measurements**”) and unambiguously identified and mostly importantly, decoupled two explicit and one implicit element of the photo-responses (Figs. 2b and 2c; Supplementary Text). In a representative trial from an Au-decorated *p-i-n* Si membrane (Fig. 2b, upper), we first noticed two ‘spiky’ features under a LED light pulse ($\sim 12.05 \text{ mW}$, $\sim 500 \mu\text{m}$ spot size) with a power density of $\sim 6 \text{ W/cm}^2$. The upward ($\sim 86 \text{ nA}$, with a transient peak current density at the pipette tip of $\sim 2700 \text{ mA/cm}^2$) and downward ($\sim -34 \text{ nA}$, transient current density of $\sim 1100 \text{ mA/cm}^2$) components correspond to capacitive charging/discharging processes at the Si/electrolyte interface (Fig. 2d, upper left, **1**). The second photo-response element is manifested as a long-lasting current with a lower amplitude (*e.g.*, $\sim 2 \text{ nA}$ for the same Au-decorated Si membrane) (Fig. 2b, upper inset), which is indicative of a Faradaic current leading to redox reactions (Fig. 2d, upper left, **2**). Metal-free *p-i-n* Si membranes only display symmetrical capacitive current spikes (Supplementary Fig. 9), with negligible Faradaic components detected from the local patch-clamp electrode. The last photo-response element is implicit and it corresponds to the local temperature elevation of the solution due to the photothermal effect from Si. In this scenario, the nonradiative recombination of carriers converts part of the input photon energy into the vibrational energy of the Si lattice (Fig. 2d, lower left, **3**), which dissipates heat through both Si and the surrounding electrolyte. Because the glass micropipette resistance is temperature-dependent, we determined the thermal dynamics by fitting the recorded patch-clamp currents at various holding potentials (**Methods**). For example, we recorded a $\sim 5.4 \text{ K}$ peak temperature rise from a nanocrystalline Si nanowire upon laser illumination ($\sim 47.1 \text{ mW}$, $\sim 5 \mu\text{m}$ spot size) at $\sim 240 \text{ kW/cm}^2$ for 10 ms (Fig. 2b, lower).

To build quantitative matrices for these three photo-response elements, we screened a library of Si-based materials to evaluate the impact of doping, surface chemistry and size (Table 1). We extracted the capacitive, Faradaic, and thermal components from the patch-clamp recordings of 16 representative Si samples (Table 1) and projected them onto three axes to decouple any individual contributions (Fig. 2c). We first considered the simplest single-crystalline *p*-type Si SOI substrate (device layer thickness: $\sim 2 \mu\text{m}$) (Fig. 2c, left). A typical experiment (LED illumination, $\sim 12.05 \text{ mW}$, $\sim 500 \mu\text{m}$ spot size, $\sim 6 \text{ W/cm}^2$) shows a small capacitive current of $\sim 50 \text{ pA}$, and a transient peak current density of $\sim 1.6 \text{ mA/cm}^2$ at the pipette tip. However, upon deposition of the intrinsic and *n*-type layers (*i.e.*, forming a *p-i-n* diode junction) (Supplementary Figs. 9 and 10), the recorded capacitive current and transient

peak current density were boosted to ~ 7400 pA and ~ 235 mA/cm², respectively (Fig. 2c, left; Supplementary Figs. 9 and 10). This significant enhancement in the capacitive component is likely due to the enhanced light absorption from the nanocrystalline layers and more efficient charge separation by the built-in electric fields across the *p-i-n* diode junction (Fig. 2d, upper left). The polarity of the capacitive currents (*i.e.*, upward at the onset of light illumination; downward at offset) in both cases stays cathodic, although the dopant types of the electrolyte-interfacing layers are different (*p*- in *p*-type SOI device layer, and *n*- in *p-i-n* multilayers). This suggests that the primary light-generated carriers accumulated on the Si surfaces are electrons, which are the minority carriers in *p*-type SOI and the majority carriers in the *p-i-n* samples, respectively. This observation is similar to the device configurations used in traditional photoelectrochemical devices, *i.e.*, *p*-type semiconductors in contact with electrolytes would experience the band bending in such a manner that drives photogenerated electrons towards the *p*-type semiconductor/electrolyte interface, while the built-in electric fields in *p-i-n* devices sweep photogenerated electrons to the *n*-type semiconductor/electrolyte interface²⁸. With a reversed doping sequence, both the *n*-type SOI substrate (~ -48 pA) and the corresponding *n-i-p* (~ -510 pA) diode junction display the opposite capacitive current polarity (Fig. 2c, left), as expected. Taken together, and consistent with the scenarios in traditional photoelectrochemical cells, the photo-carriers that accumulate at the Si surfaces upon light illumination are minority carriers in uniformly doped cases (*i.e.*, *n*- or *p*-type Si) and majority carriers when *p-i-n* or *n-i-p* junctions are formed. Finally, in these metal-free samples, the Faradaic and thermal components are negligible *e.g.*, ~ 7 pA and ~ 0 K as peak values for *p-i-n* multilayered sample (Supplementary Fig. 9, under ~ 6 W/cm² LED illumination) so the dominant photo-response element in metal-free Si membranes is the capacitive current.

As shown in the Au-decorated *p-i-n* Si membrane, the Faradaic current can reach ~ 2 nA (Fig. 2b, upper inset), suggesting a means of charge injection into the solution (Fig. 2d, upper left). We next explored multiple metals that were commonly exploited catalysts for photoelectrochemistry (*e.g.*, Au, Ag, and Pt) by electroless deposition of nanoparticles onto *p-i-n* Si surfaces²⁹ (Supplementary Figs. 3–5, 11–13). In all experiments, the introduction of metal species promoted both the capacitive and the Faradaic elements (Fig. 2c, middle; Supplementary Figs. 11 and 13), with good stabilities over 1000 repetitive illuminations (Supplementary Fig. 12), likely due to the fact that certain metals can more efficiently collect and solution-inject the photo-generated carriers (as opposed to carrier recombination in bulk Si). Among all the conditions tested, Au prepared by immersion of the *p-i-n* multilayered membrane in a 1 mM HAuCl₄ solution yielded the highest capacitive (~ 86 nA) and Faradaic (~ 2 nA) currents (Fig. 2c, middle). The thermal components under ~ 6 W/cm² LED illumination were negligible in all metal-decorated Si membranes.

Since single cell or subcellular studies require highly localized interrogation, we measured the laser-induced (~ 47.1 mW, ~ 5 μ m spot size, ~ 240 kW/cm²) photo-responses of Si materials with variable lateral dimensions. We observed decreased electrical/enhanced thermal elements with reduced sizes of *p-i-n* Si membranes (Fig. 2c, right; Supplementary Fig. 14). In the case of intrinsic nanocrystalline Si nanowire, the nano-confinement effect led to the highest photothermal response (~ 5.4 K peak temperature change) with negligible capacitive and Faradaic components (Fig. 2b, lower).

Recommended materials and devices for multiscale biointerfaces

Our physicochemical measurements (Fig. 2; Fig. 1a, **Selection II**) highlight *p-i-n* diode junction-enhanced capacitive currents, metal-enhanced capacitive and Faradaic currents, and nano-confinement-enabled thermal responses (Table 1; Fig. 2d, middle), all in freestanding configurations. For the present biointerface studies (Fig. 1a, lower right; Figs. 3 and 4), most Si materials such as a simple *p-type* Si membrane or *p-i-n* Si multilayers with small lateral dimensions ($< 500 \mu\text{m}$), will not be considered given that their photo-response components are small (Table 1, with lower color intensity; Fig. 1a, excluded materials from **Selection II**). We focused on the intrinsic nanocrystalline Si nanowires for intracellular and the related intercellular probing, and only used the photothermal effect. For single cell or small tissue level inter- and extracellular studies, we primarily explored a light-induced capacitive effect, *i.e.*, we used a *p-i-n* Si multilayered membrane where the biological invasiveness from capacitive electrochemical currents are usually minimal³⁰. Finally, given the organ level modulation would require the strongest stimuli, we used the Au-coated *p-i-n* Si multilayered membrane for *in vivo* studies (Fig. 2d, right). Similar to the electrical stimulation of excitable tissues, where both capacitive and Faradaic currents take place at the electrode/electrolyte interface³⁰, the Au-coated Si surfaces can deliver similar signals to the biological system for efficient tissue modulations.

Organelle-level biointerfaces

We first considered Si nanowires for intracellular stimulation biointerfaces (Fig. 3) because it is an unexplored domain that is beyond the previously studied intracellular sensing or delivery. In a primary culture of neonatal rat dorsal root ganglia (DRG) and associated satellite glia, we noticed a cell-type-specific overlapping of nanocrystalline Si nanowires after ~ 24 hours of coculturing (by glial fibrillary acidic protein (GFAP)/NeuN staining in Fig. 3a and Supplementary Fig. 15; by S-100/Neurofilament staining in Supplementary Fig. 16). Statistical analysis of the nanowire-cell colocalization revealed that $\sim 87\%$ of total nanowires overlapped with glial cells, $\sim 3\%$ with neurons, and $\sim 10\%$ stayed in the extracellular space (Fig. 3a, lower). Perinucleus clustering, rather than random intracellular distributions, of the colocalized nanowires suggests the internalization of these nanowires^{14,24}. Additionally, the presence of bent nanowires following the contours of a few glial cell membranes implies strong mechanical interactions between cells and nanowires¹⁴. As suggested by a recent study that label-free nanowires can be internalized through a phagocytosis pathway²⁴, the fact that glial cells (versus neurons) do have phagocytic activities supports the observed selective glial internalization³¹. As a result, we studied the control of glial activities with internalized nanocrystalline nanowires as the remotely-controlled stimulators. To this end, we illuminated an intracellularly-bounded nanowire with a laser pulse (592 nm, ~ 14.4 mW, ~ 237 nm spot size, 1 ms) in the middle of a time-lapse calcium imaging series (Fig. 3b; Supplementary Figs. 8b and 17). Upon light illumination, the glial cell of interest, with the nanowire inside, experiences a fast calcium concentration increase followed by a slow decay. Since the cell is being stimulated intracellularly, the observed calcium dynamics are likely related to the release of calcium from internal storage organelles, *e.g.*, endoplasmic reticulum (ER) and mitochondria, rather than the calcium influx through ion channels at the plasma membrane, and therefore may be extended to other

non-excitable cells (Supplementary Fig. 18). As evidenced by the patch-clamp measurement, nanocrystalline nanowire exhibits a pronounced photothermal effect which results in a transient and localized temperature increase of surrounding cytosol and organelles following the laser pulse. This heating effect can either generate reactive oxygen species (ROS)³² or transiently depolarize/perforate ER and mitochondrial membranes³³, all of which can trigger the release of calcium from its reservoir to the cytosol. Nevertheless, the same glial cell calcium dynamics can still be modulated repetitively (Supplementary Figs. 19 and 20), indicating the minimal invasiveness of the intracellular stimulation method. Moreover, we not only observed the induced intracellular calcium flux from the glia under direct stimulation, but also the intercellular calcium wave propagation to both neighboring glia and DRG cells (Fig. 3b). The selective uptake of nanowires by glia and the existence of glia-glia/glia-neuron communication suggest possible remote cellular modulations through naturally-occurring intercellular junctions. Finally, the cellular and subcellular dynamics can be exploited for motile modulation biointerfaces (Supplementary Fig. 21).

Since Si nanowires can also display active transport along microtubules²⁴, we next explored the possibility of using nanocrystalline Si nanowires as a dual-role intracellular biophysical tool, *i.e.*, a calcium modulator and a marker for motor protein-microtubule interactions. We simultaneously tracked the location of a single nanowire (*i.e.*, a transport marker) in a glial protrusion and monitored the nearby calcium dynamics, following a remote laser illumination of a different nanowire (*i.e.*, a calcium modulator) to initiate a calcium flux within a network (Fig. 3c, first from left). The dynamics of local calcium concentration and the transverse distance of the nanowire, as well as the overlaid time series for both the calcium wave front and the nanowire center (Fig. 3c, first from right), together suggest a calcium-triggered directional transport of intracellular cargo in the current case. Additionally, mean-squared displacement (MSD) analysis (**Methods**) reveals correlated nanowire transport modes with the local calcium dynamics, *i.e.*, from random or restricted diffusions (diffusive exponent, $\alpha \sim 1$) without elevated intracellular calcium, to an active transport (diffusive exponent, $\alpha \sim 2$) after the calcium wave front reached the original nanowire location (Fig. 3c, first from right; Supplementary Fig. 22). The nanowire transport along the glia protrusion is anterograde, *i.e.*, kinesin-based. The motor protein kinetics are typically enhanced by increased adenosine triphosphate (ATP) activities³⁴, which may be triggered by the elevation of intracellular calcium concentration^{35,36}.

Besides serving as an intracellular calcium modulator and a transport marker, the photothermal properties of nanocrystalline Si nanowires may be explored to induce a photoacoustic effect for biomechanical manipulation at the subcellular level. To assess this, we chose human umbilical vein endothelial cells (HUVEC), which are active in the phagocytosis of silicon nanowires²⁴ and have well-studied microtubule networks. Nanocrystalline Si nanowires are trapped in the microtubule meshes after coculturing with HUVEC for ~ 24 hours (Supplementary Fig. 23). When a laser pulse (592 nm, 1 ms, ~ 2.09 mW, ~ 211 nm spot size) was introduced to the nanowire, the surrounding microtubules were rapidly repelled and formed a void space near the nanowire (Fig. 3d; Supplementary Fig. 23), suggesting a shock-wave generation through a photoacoustic effect³⁷. Besides intracellular microtubule networks, Si nanowires can also interface with intercellular

conduits, where microtubules form compact bundles. Upon laser illumination of the entangled single nanowire (592 nm, 1 ms, ~ 2.55 mW, ~ 211 nm spot size), the bundled microtubules are broken up immediately (Fig. 3e), possibly through a shock-wave-mediated, mechanically-induced microtubule depolymerization³⁸. The optically-triggered, and nanowire-enabled mechanical manipulation of cytoskeletal structures may serve as a new tool for the study of intra- and intercellular dynamics where a remote structural manipulation of subcellular structures is desired.

Control experiments without nanowires did not yield any of these intra- or intercellular observations. Moreover, the importance of using silicon nanowires instead of other nanostructures (*e.g.*, Au nanoparticles or nanorods) is due to the following: (1) silicon nanowires can be at least partially exposed in cytosol upon phagocytic cellular entrance²⁴, (2) silicon has only a moderate photothermal effect (compared to, *e.g.*, that of Au) (Figs. 2b and 2c; Supplementary Fig. 14) such that the confocal imaging light source itself will not cause heating from the nanostructures, and (3) the high aspect ratio of silicon nanowires enables their axial alignment with respect to the cytoskeletal filaments (Figs. 3d and 3e; Supplementary Fig. 23).

Single-cell-level and small-tissue-level biointerfaces

In addition to the nanowire-enabled intracellular biointerfaces, we also explored the possibility of implementing extracellular modulations with larger Si structures to match the sizes of cultured cellular assemblies and even small tissues. We first tested *p-i-n* Si diode junctions because their significantly larger light-induced photocurrents (Figs. 2c and 2d; Table 1) may be readily sensed by cells that are attached directly^{39–41}. Patch clamp and calcium imaging studies show that DRGs cultured on Si diode junctions can be stimulated with focused light pulses (Supplementary Figs. 8a, 8b and 24) individually or sequentially in a cellular assembly, with a high spatiotemporal resolution and minimal invasiveness (Supplementary Figs. 25–27). A pre-immersion of Si substrate in buffer solution for two weeks yielded a two-fold increase in threshold laser intensity (Supplementary Fig. 28).

We next explored an *in vitro* test on acute *ex vivo* brain slices from mouse neocortex interfacing with a distributed *p-i-n* Si mesh (Fig. 1e) to evaluate the feasibility of the optically-controlled neuromodulation of a small tissue (Fig. 4a, left; Supplementary Fig. 8c). A whole-cell recording in voltage-clamp mode was made in a cortical pyramidal neuron located in the middle of the 300- μ m thick slice while the Si mesh was in contact with the bottom face of the slice (Fig. 4a, lower right). Immediately after flashing a focused laser beam on the Si mesh (473 nm, 1 ms, ~ 2 mW, ~ 57 μ m spot size) (Fig. 4a, upper right), there were two fast electrical artifacts with opposite polarities (Fig. 4b, marked by #), likely due to the capacitive charging and discharging of the Si/electrolyte/cell interfaces (Fig. 2). Excitatory postsynaptic currents (EPSCs) (Fig. 4b, marked by stars) were then recorded arriving with short latency and low jitter after the photoelectric artifacts. Laser illumination of the Si mesh evoked spikes not in the patched neuron but in one or more presynaptic neurons in the slice, which provided the excitatory synaptic input to the recorded postsynaptic neuron. That the patched cell is not triggered to spike may be due to a combined reason that the cell is far away from the Si under illumination (difference in depth

of $\sim 150 \mu\text{m}$) and only the immediately neighboring cells may be substantially activated by the localized laser stimulation. The ability to photo-activate presynaptic neurons and detect synaptic inputs with little or no direct activation of the recorded postsynaptic neuron is advantageous for photostimulation mapping of neuronal circuits^{42,43}. The Si mesh in conjunction with focused laser scans thus suggests the potential of this new methodology for *ex vivo* analysis of brain circuit organization.

Organ-level biointerfaces

Finally, we interfaced an Au-decorated and Si mesh-based flexible membrane with a mouse brain to control the brain activities, *e.g.*, the ability to sense, interpret, and act upon the environment. The bilayer device layout, consisting of the Au-decorated Si mesh and the holey PDMS membrane (Fig. 1e), allows the device's conformal attachment to the brain cortex (Supplementary Fig. 29) with sufficient adhesion (Supplementary Fig. 30). We chose an Au decorated surface due to its large capacitive and Faradic current components. We performed the *in vivo* photostimulation experiment using an extracellular linear array to record neural activities following laser illuminations (473 nm, $\sim 5 \text{ mW}$, 100 ms, $\sim 216 \mu\text{m}$ spot size) of the silicon mesh attached to the somatosensory cortex of an intact mouse brain (Fig. 4c; Supplementary Figs. 8d and 31). In individual trials of the test, enhanced neural activities were evident during the illumination period—with significant photoelectric artifacts at the light onsets and offsets (Fig. 4d). The detected spike-like events using criteria of a high pass filter of 800 Hz and a threshold of 5 times the noise level standard deviation (SD) exhibit waveforms typical of natural extracellular electrophysiological recordings (Fig. 4e)^{44–46}. Peristimulus time histograms (PSTH) from 16 channels (Fig. 4f) (with the depths between $200 \mu\text{m}$ and $900 \mu\text{m}$ below the pia) clearly show the illumination-triggered neural responses, in the upper and middle layers of the sensorimotor cortex⁴⁷. Statistical analyses further revealed that the evoked responses have a significantly higher rate than the spontaneous ones (Supplementary Fig. 31). In addition, stronger short-latency activity was observed in more superficial neurons, which were closer to the silicon mesh and thus may be more easily activated. Over time, activity spreads to deeper layers (Fig. 4f), consistent with the propagation of signals through the local and long-range cortical circuits, similar to patterns observed with optogenetic photostimulation⁴⁸. Moreover, parametric stimulations show a colligative behavior in that the activated neural response rate is correlated with the stimulation power (Fig. 4g; Supplementary Fig. 32), which is essential to the predictive control of the Si mesh as a precise neuromodulator. Finally, based on the electrophysiology studies, we tested if the Si mesh-enabled photostimulations of the brain cortex can trigger movements of anesthetized mice. When we illuminated a Si mesh attached to the right side of the forelimb primary motor cortex, the contralateral left forelimb of the mouse showed a large, rapid up-and-down (flexion-extension) movement shortly after the stimulation (Figs. 4h and 4i; Supplementary Fig. 33; Supplementary Videos 1 and 2). Conversely, photostimulation of the left forelimb motor cortex evoked movements of the contralateral right forelimb (Supplementary Fig. 34; Supplementary Videos 3 and 4). In some cases, small ipsilateral forelimb movements were also evoked (Figs. 4h and 4i), possibly reflecting activation of uncrossed (ipsilateral) corticospinal projections and/or interhemispheric (callosal) circuits. Overall, our observations of cortically evoked movements are consistent

with the functional organization of the forelimb motor control system⁴⁹ (Supplementary Fig. 35). Given Si membranes yield minimal photothermal effect (Fig. 2 and Table 1), we believe the combined light-induced capacitive and Faradaic effects from Si induce the observed brain activities and the animal behaviors.

Discussion

Si-based materials and devices are uniquely suited for light-controlled multi-scale biointerfaces (Supplementary Table 1). First of all, as a semiconductor, Si can induce both the photothermal and photoelectric (including capacitive and Faradaic) processes, whereas metals such as Au display primarily the photothermal effect when plasmonic heating becomes effective (which limits its potential applications for certain biophysical and biomedical studies). Similarly, although carbon and Pt-based materials have been the major systems in electrochemical and related biomedical research, they typically do not display prominent or controllable photoelectric properties which makes them challenging for the photoelectric biointerfaces shown in this work. Secondly, both the industrial and synthetic processes for Si are well established, which enables the facile fabrication of various Si forms across multiple length scales. For other semiconductors, such as InP and GaP, although they can also exist in forms similar to Si, their fabrication processes typically require higher costs and more sophisticated instrumentation. Additionally, for light-controlled semiconductor-based biointerfaces, the material bandgap is critical as it determines the wavelength range at which the device can be operated. Unlike Si, which absorbs light up to the near infrared (NIR) region, other common semiconductors, *e.g.*, TiO₂, GaP, ZnO, and CdS, have larger bandgaps and therefore can only work in the ultraviolet-blue region. Finally, Si is not only biocompatible but also biodegradable, which may be important for the future implementation of transient biointerfaces.

We have shown that Si-based materials can behave as optically controlled freestanding devices that modulate brain activities and simple animal behaviors. These are promising complements to two other major neuromodulation techniques, *i.e.*, electrical stimulation and optogenetics. We first argue that traditional electrode-based neuromodulation suffers from a few drawbacks that may be addressed by photostimulation. For electrical stimulation, external wirings are required to deliver electrical signals, which would cause additional inflammatory responses in the targeted tissue. Furthermore, the location of the device is fixed by its implantation site and therefore the device, even with advanced materials and layout designs, cannot function in an adjustable manner for the high-resolution stimulation of arbitrary regions. Photostimulation, on the other hand, does not require excessive wirings and can be operated with higher flexibility and spatial resolution to implement multiplexed and patterned stimulations on a large scale (*i.e.*, the location of stimulation is fully determined by the location of light spots, which can be arbitrarily aimed). Optogenetics, although having the benefit of photostimulation and excellent cellular targeting, requires genetic alteration of the targeted cells or tissue. Existing genetic engineering toolboxes are mostly developed for small animals like rodents, therefore large animals such as non-human primates require additional technical advances in optogenetics^{50–52}. Additionally, ethical issues of altering human genomes would need to be addressed before optogenetics could be adopted in clinical trials. As an alternative, the Si-based neuromodulation approach

combines certain advantages of both electrical stimulation (*i.e.*, non-genetic) and optogenetics (*i.e.*, optically-controlled), offering new opportunities to modulate neural activities in non-human primates or even human subjects.

Looking forward, our current system represents only one step towards remotely-controlled non-genetic biological modulations. The future development of other material systems that can effectively transduce external physical inputs (*e.g.*, optical, electrical, magnetic, and ultrasonic) into output signals (*e.g.*, electrical, thermal, and mechanical) that are recognizable by the biological systems—in combination with advanced imaging and recording techniques—may ultimately lead to an integrated system for multimodal biological modulations⁵³.

Methods

Synthesis of silicon-based materials.

Silicon (Si) materials (*p*-type/intrinsic/*n*-type diode junctions and intrinsic-intrinsic coaxial nanowires) were prepared using a chemical vapor deposition (CVD) method. In a typical synthesis of a *p-i-n* diode junction, a silicon-on-insulator (SOI) wafer (Ultrasil, USA, device layer, *p*-type, (100), 0.001–0.005 Ω -cm, 2 μ m; buried oxide layer, 1 μ m; handle layer, *p*-type, (100), 1–20 Ω -cm, 650 μ m) was used as the substrate for subsequent deposition of intrinsic and *n*-type layers. The native oxide on the SOI wafer was removed with hydrofluoric acid (HF, 49%, Sigma-Aldrich, USA) right before placing the substrate inside a quartz tube for evacuation. Each of the intrinsic and *n*-type Si layers was deposited under 650 °C and a chamber pressure of 15 Torr for 20 min. During the intrinsic layer deposition, the flow rates of hydrogen (H₂) and silane (SiH₄) were set as 60 and 0.3 standard cubic centimeters per minute (sccm), respectively. The *n*-type layer was deposited with the same flow rates of H₂ and SiH₄ during the intrinsic layer growth plus a 1.5 sccm flow rate of the dopant gas, phosphine (PH₃, 1000 ppm in H₂). Measured conductivities of individual layers are ~ 0.45 Ω -cm for the *p*-type single crystalline substrate (~2 μ m in thickness), ~ 149 k Ω -cm for the intrinsic polycrystalline layer (~ 140 nm in thickness), and ~ 540 Ω -cm for the *n*-type polycrystalline layer (~ 190 nm in thickness), respectively.

The nanocrystalline Si nanowire (intrinsic core/intrinsic shell) was synthesized from a two-step process involving an initial growth of a thin intrinsic backbone and a subsequent deposition of a thick intrinsic shell. The core was grown with a gold (Au) nanocluster-catalyzed CVD process where Au colloidal nanoparticles (Ted Pella Inc., USA, 50 nm in diameter) were deposited onto a Si (100) substrate (Nova Electronic Materials, *n*-type, 0.001–0.005 Ω -cm) as the catalyst. The growth was maintained at 470 °C and 40 Torr for 20 min. The flow rates of H₂ and SiH₄ were controlled as 60 and 2 sccm, respectively. After the intrinsic nanowire core growth, the SiH₄ flow was switched off and the chamber was kept under a H₂ atmosphere (60 sccm, 15 Torr) until the temperature ramped up to 600 °C for the subsequent shell deposition. The H₂ atmosphere was used to minimize Au diffusion. The intrinsic shell was deposited with flow rates of H₂ and SiH₄ at 0.3 and 60, respectively, and a chamber pressure of 15 Torr for 40 min.

The metal-decorated Si diode junctions were prepared with an electroless deposition method. In general, the as-synthesized *p-i-n* diode junctions were dipped into a mixture of metal-containing solutions (chloroauric acid (HAuCl₄), potassium tetrachloroplatinate(II) (K₂PtCl₄), silver nitrate (AgNO₃); 0.01 mM, 0.1 mM, 1 mM) and 1% HF for 3 min at room temperature.

Fabrication of Si-based flexible devices for *in vivo* experiments.

The device fabrication process was divided into two parallel steps including the preparations of both distributed Si meshes and porous polydimethylsiloxane (PDMS, Corning, USA) membranes (Supplementary Fig. 6). The fabrication of distributed Si meshes were performed with a combination of photolithography and etching techniques. In brief, a bilayer of undercut (MicroChem, USA, LOR-3A) and photoresist (MicroChem, USA, SU-8 2005) was spin-coated on the as-synthesized *p-i-n* diode junction SOI wafer. A mesh structure of SU-8 was patterned with a standard photolithography process consisting of ultraviolet (UV) light exposure (200 mJ/cm²) and developing (MicroChem, USA, SU-8 developer). The as-patterned SU-8 mesh served as an etch mask for the subsequent reactive ion etching (RIE) of Si. The unprotected *p-i-n* Si layers (~ 2.3 μm) were removed after 10 min of etching (radiofrequency (RF) power, 100W; inductive-coupled plasma (ICP) power, 400 W) with a gaseous mixture of tetrafluoromethane (CF₄, 45 sccm) and argon (Ar, 5 sccm). The SU-8 protection layer was lift-off by dissolving the undercut LOR-3A layer in Remover-PG (MicroChem, USA). A final wet etching of the oxide layer with 49% HF was performed to release the as-patterned Si diode junction.

The PDMS membrane was prepared using a soft-lithography technique. In general, a SU-8 pillar array (~ 120 μm in height) was patterned on a Si substrate with the standard photolithography process and served as the soft-lithography mold. A layer of PDMS (precursor: curing agent ratio = 10:1) was then spin-coated onto the SU-8 mold and cured at 80 °C overnight. The as-cased PDMS layer was finally released in hexane (Fisher Scientific, USA) to get the holey structure. The distributed Si mesh was then transferred onto the holey PDMS membrane to form the entire device (Supplementary Fig. 6).

Finite element analysis (FEA) of stress distribution.

The FEA was performed using COMSOL Multiphysics 5.3 (COMSOL Inc. USA). A 2D plate model in the structural mechanics module was set for the simulation. The von Mises stress distribution was calculated after a point displacement of 500 μm in the *z* direction at the device center while fixing four edge points.

Electron microscopy.

A transmission electron microscope (TEM, JEOL, Japan, JEM-3010) and an aberration-corrected scanning transmission electron microscope (STEM, JEOL, Japan, JEM-ARM200F) were used to image the cross-sectional structures of both the pristine *p-i-n* Si diode junction and the gold-decorated one. X-ray energy dispersive spectroscopy (XEDS) maps were using the JEM-ARM200F, which was equipped with an Oxford X-Max^N 100TLE windowless SDD X-ray detector (Oxford Instruments, UK). Selected area electron diffraction (SAED) patterns were taken using the JEM-3010. TEM cross-sectional specimen

preparations were carried out by controlled tripod polishing^{54,55} followed by liquid-nitrogen-cooled Ar ion millings using a Fischione 1050 TEM mill (Fischione Instruments, USA). A 4-kV ion milling was used to further thin the specimen and a final 0.5 kV milling was performed to remove surface damages. A scanning electron microscope (SEM, Carl Zeiss, Germany, Merlin) was used to image the top view of the gold-decorated Si diode junction, the cross-sectional view of the diode junction, and the flexible device made of the distributed Si mesh and the holey PDMS membrane. Nanocrystalline Si nanowires were sonicated in isopropanol (Sigma-Aldrich, USA) and then dispersed over copper grids (Ted Pella Inc., USA, Lacey Formvar/Carbon, 200 mesh) for side-view imaging using a TEM (JEOL, Japan, JEM-3010). The cross-sections of the nanowires were prepared by ultramicrotomy. In general, Si nanowires were embedded in epoxy resins which were then solidified at 60 °C for 24 h. Thin epoxy sections of ~100 nm were cut using a ultramicrotome (Ultracut E, Reichert-Jung, USA), collected on lacey carbon grids (Ted Pella Inc., USA), and imaged using the same TEM.

X-ray photoelectron spectroscopy (XPS).

XPS data were collected using ESCALAB 250 Xi (Thermo Scientific, USA) with a monochromatic Al $K\alpha$ ($h\nu = 1486.6$ eV) excitation. The diameter of the X-ray beam was 500 μm . The survey scans were performed with a pass energy of 160 and a step size of 1 eV whereas the high-resolution scans were done with a pass energy of 50 and step size of 0.1 eV. The correction of the XPS spectra for charge accumulation was performed using the Si $2p$ peak (binding energy = 99.4 eV). The Si $2p$ peaks were fitted using a Shirley background with G/L 30% for Si^0 and pure Gaussian for Si^{4+} . Peak fitting for the Au $4f$ signal was determined with a linear background G/L 30%, asymmetric 0.9, and a height factor of 0.75. With these parameters the FWHM range for the gold was from 0.8 eV to 1.25 eV.

Si photo-response measurements.

For the photo-response measurements, a standard patch-clamp setup was employed. In particular, an upright microscope (Olympus, Japan, BX61WI) with a $20\times/0.5$ NA water immersion objective was used to deliver light pulses from a light emitting diode (LED, M530L3, Thorlabs, USA, 530 nm, ~ 500 μm spot size) or a laser (Laserglow, Canada, 532 nm, diode-pumped solid-state laser, ~ 5 μm spot size). The light pulses were controlled by transistor-transistor logic (TTL) signals (10 ms) delivered from a digitizer (Molecular Devices, USA, Digidata 1550). Voltage-clamp protocols were done by an Axopatch 200B amplifier (Molecular Devices, USA), controlled by pClamp software (Molecular Devices, USA). Glass pipettes were pulled in a flaming/brown type micropipette puller (Sutter Instrument, USA, P-97) for a final resistance of ~1 M Ω when filled with $1\times$ phosphate buffered saline (PBS, Fisher Scientific, USA) solution. In a typical measurement, a Si material was immersed in the same PBS solution where the pipette tip was positioned in close proximity to the Si surface (~ 2 μm). The ionic currents across the pipette tip were recorded in the voltage-clamp mode where the holding levels of the pipette were adjusted using the pipette offset knob. The individual quantities of each photo-response, *i.e.*, capacitive, Faradaic, and thermal, were calculated by fitting the plot of the light-induced current amplitude (I_{light}) over the holding level (I_0). At a given time point, the slope of the $I_{\text{light}}-I_0$ plot represents the photothermal response whereas the intercept of the plot is

contributed by the photoelectric responses. Within the photoelectric responses, the capacitive current is defined as the maximal current amplitude after the light onset while the Faradaic current is defined as the current amplitude at the time point of 8.5 ms since illumination starts. The amplitude of the photothermal-induced local temperature increase of the solution was calculated after the calibration of the pipette resistance. After the photo-response measurement, the same micropipette was placed into another dish of pre-heated PBS with an initial temperature of about 50 °C. A thermocouple was positioned close to the pipette tip during the temperature measurement. A calibration curve was created, based on the pipette resistance changes in the range between 50 °C and 20 °C, which was then used in conjunction with the $I_{\text{light}}-I_0$ curve to estimate the local temperature increase.

Mammalian cell cultures.

All animal protocols used were in accordance to the policies of the University of Chicago and were approved by the Institutional Animal Care and Use Committees (IACUC).

1) Dorsal root ganglia (DRG) culture.

DRGs were extracted from decapitated P1-P3 Sprague-Dawley rats (Charles River Laboratories, USA) and were placed immediately in ice-cold Dulbecco's modified eagle medium (DMEM/F12, Life Technologies, USA). The ganglia were then transferred to a 2.5 mg/mL trypsin solution (Worthington, USA) in Earle's balanced salt solution (EBSS, Life Technologies, USA) and digested for 20 min in a 37 °C shaker with a speed of 144 rpm. Afterwards, the cells were centrifuged and the supernatant was replaced with EBSS supplemented with 10% fetal bovine serum (FBS) (ATCC, USA). After the mechanical trituration with pipetting, the cell suspension was centrifuged again and the supernatant was replaced with DMEM/F12 containing 5% FBS. Next, cells were seeded onto poly-L-lysine (PLL, Sigma-Aldrich, USA) coated substrates, *e.g.*, glass-bottom Petri dishes, *p-i-n* diode junction SOI wafers, and allowed 30 min for cell adhesion. Finally, the dishes were filled with DMEM/F12 supplemented with 5% FBS, 100 U/ml penicillin (Sigma-Aldrich, USA), and 100 µg/ml streptomycin (Sigma-Aldrich, USA), and cultured in a 37 °C incubator with 5% carbon dioxide (CO₂) until used for experiments.

2) Other cell lines.

Human umbilical vein endothelial cells (HUVEC, Life Technologies, USA) and U2OS cells (ATCC, USA) were cultured on glass-bottomed Petri dishes and passaged following standard procedures from the vendors.

3) Cellular internalization of Si nanowires.

In all cell cultures, intrinsic nanocrystalline Si nanowires were introduced and allowed for coculturing for at least 24 hours. Specifically, nanowire suspensions in different cell culture media were prepared by extensively sonicating small pieces of nanowire growth substrates (~ 2 mm × 2 mm) in culture media for 2 min. The as-made nanowire suspensions were added to the cultures in a drug-like fashion (~ 10 µL of suspension per 1 mL of medium). Before all experiments, cells were washed three times with fresh media.

Immunofluorescence labeling of the DRG culture.

DRG and nanowire cocultures were first fixed with 4% paraformaldehyde in PBS (Alfa Aesar, USA, with magnesium and ethylene glycol tetraacetic acid) for 10 min at room temperature. After rinsing in PBS, cells were then permeabilized with 0.1% Triton X-100 in PBS (Sigma Aldrich, USA) for another 10 min at room temperature. Following blocking with 1.5% bovine serum albumin (BSA, Sigma-Aldrich, USA) in PBS for 1 hour, the cells were incubated with primary antibodies (GFAP (GA5) Mouse mAb, 1:300 in 1.5% BSA-PBS for glia; NeuN (D4G40) XP Rabbit mAb, 1:50 in 1.5% BSA-PBS for neuron, Cell Signaling, USA) at room temperature for 1 hour. After washing, secondary antibodies (Goat anti-Mouse IgG (H+L) Superclonal Secondary Antibody, Alexa Fluor 647, 1:150 in 1.5% BSA-PBS for glia; Goat anti-Rabbit IgG (H+L) Secondary Antibody, Alexa Fluor 488, 1:150 in 1.5% BSA-PBS for neuron, Life Technologies, USA) were finally applied. Since NeuN is expressed in the neuronal nucleus, another set of biomarkers, *i.e.*, S-100 for glial cells and Neurofilament for neurons, were stained to test if nanowires were colocalized with neuronal cytoplasm. The staining follows the same procedure as the GFAP/NeuN staining with slight differences in the dilution ratios of the antibodies. In particular, cells after fixation and permeabilization were incubated with primary antibodies (S100 Polyclonal Antibody, 1:100 in 1.5% BSA-PBS for glia, Life Technologies, USA; Neurofilament-H (RMdO 20) Mouse mAb, 1:200 in 1.5% BSA-PBS for neuron, Cell Signaling, USA) at room temperature for 1 hour. After washing, secondary antibodies (Goat anti-Mouse IgG (H+L) Cross-Adsorbed Secondary Antibody, Alexa Fluor 647, 1:200 in 1.5% BSA-PBS for neuron; Goat anti-Rabbit IgG (H+L) Cross-Adsorbed Secondary Antibody, Alexa Fluor 488, 1:200 in 1.5% BSA-PBS for glia, Life Technologies, USA) were finally applied. After washing in PBS, the as-labelled cells were imaged using a confocal laser scanning microscope (Leica, Germany, SP5 II STED-CW) with Si nanowires being imaged simultaneously with the scattered light. The staining results using GFAP and NeuN as the markers were included in Fig. 3a and Supplementary Fig. 15 while the staining results using S-100 and Neurofilament were included in the Supplementary Fig. 16.

Calcium imaging.

Cells, either cocultured with intrinsic nanowires or cultured on *p-i-n* diode junctions, were stained with 2 μ M of Fluo-4 AM (Life Technologies, USA) for 30 min at 37 °C and washed three times with dye-free culture media before imaging. The as-stained cells were imaged using the same Leica SP5 confocal microscope. In a typical experiment, a laser pulse (1 ms, 592 nm) was delivered to the nanowire/cell of interest in the middle of a calcium imaging time series. The cellular fluorescence intensity over time was then analyzed using ImageJ software (National Institutes of Health, USA).

LIVE/DEAD assay.

Cells, either cocultured with intrinsic nanowires or cultured on *p-i-n* diode junctions, were stained with 2 μ M of calcein AM (Life Technologies, USA) and 4 μ M of ethidium homodimer-1 (Life Technologies, USA) for 30 min at room temperature. The as-stained cells were imaged using the same Leica SP5 confocal microscope. In a typical experiment, a laser pulse (1 ms, 592 nm) was delivered to the nanowire/cell of interest in the middle of an

imaging time series. Live cells will stay green throughout the entire sequence while dead cells will be stained red.

Intracellular transport.

For the intracellular transport study, a custom-written program in Python was run to automatically track the nanowire and calcium wave-front locations in all 100 frames. To distinguish between different modes of Si nanowire transport, we used a rolling frame mean squared displacement (MSD) metric, where the MSD is the average distance that a particle travels as a function of lag time, given by:

$$\text{MSD} = \langle \Delta r^2(\tau) \rangle = q\tau^\alpha.$$

where r , τ , q , and α are the nanowire displacement, lag time, diffusion coefficient and the 'diffusive exponent' respectively. The diffusive exponent, α , can be used as a metric of transport properties, distinguishing between Brownian diffusion ($\alpha = 1$), restricted diffusion ($\alpha < 1$), and active transport ($\alpha > 1$) processes. For the plotting, rolling α values were used to yield an estimate of the local transport behavior.

Live cell microtubule dynamics.

In a typical experiment, HUVEC cells with internalized Si nanowires were stained with 200 nM of SiR-tubulin (Cytoskeleton, USA) at 37 °C for 1 hour. 10 μM of verapamil (Cytoskeleton, USA) was also added to inhibit the efflux of the SiR-tubulin. Three times of washing with the dye-free medium was applied before imaging. Under the same Leica SP5 confocal microscope, the Si nanowire of interest was illuminated with a 592 nm laser pulse (1 ms) and the subsequent microtubule dynamics were recorded. The as-recorded videos were processed and analyzed using ImageJ including the analysis of microtubule bounded areas and intercellular conduit lengths over time, and the generation of kymographs.

Electrophysiology and photo-stimulation experiments.

All animal protocols used were in accordance to the policies of the University of Chicago and Northwestern University, approved by the Institutional Animal Care and Use Committees (IACUC), and followed the animal welfare guidelines of the Society for Neuroscience and National Institutes of Health.

1) DRG culture on Si diode junctions.

Before the experiment, FBS supplemented DMEM/F12 in the culture dish was rinsed three times with the extracellular recording solution (in mM: NaCl 132, KCl 4, MgCl₂ 1.2, CaCl₂ 1.8, HEPES 10, glucose 5.5; pH 7.4). Desired neurons were patched with a ~ 2 M Ω pipette, filled with the intracellular pipette solution (in mM: NaCl 10, KCl 150, MgCl₂ 4.5, EGTA 9, HEPES 10; pH 7.3). Voltage recordings were made in current-clamp mode using the same setup for the photo-response measurements. Suprathreshold current injections were first delivered to the patched neuron to assess its excitability. Laser pulses (532 nm) with incremental durations were delivered subsequently to excite the cell.

2) Brain slice with Si diode junctions.

Wild-type mice (C57BL/6, female and male; Jackson Laboratory, USA) were bred in-house. Mice were 6–9 weeks old at the time of the slice experiments.

a) Slice preparations.—Mice were euthanized by anesthetic overdose and decapitation. Brain slices were made in a 4 °C cutting solution (in mM: 110 choline chloride, 11.6 sodium L-ascorbate, 3.1 pyruvic acid, 25 NaHCO₃, 25 D-glucose, 2.5 KCl, 7 MgCl₂, 0.5 CaCl₂, 1.25 NaH₂PO₄; aerated with 95% O₂/5% CO₂) using a vibratome (VT 1200S, Leica, Germany) to make 250 μm thick slices. The slices were transferred to an artificial cerebrospinal fluid (ACSF, composition in mM: 127 NaCl, 25 NaHCO₃, 25 D-glucose, 2.5 KCl, 1 MgCl₂, 2 CaCl₂, 1.25 NaH₂PO₄; aerated with 95% O₂/5% CO₂) and maintained at 34 °C for 30 min. The slices were then returned to room temperature for at least 1 hour prior to the recordings.

b) Electrophysiology.—Distributed Si meshes were placed in a recording chamber under an upright microscope (BX51WI; Olympus, Japan), which is equipped with a video camera (Retiga 2000R; QImaging, Canada). Brain slices were then transferred on top of the Si meshes to form contacts. Slices were visualized by bright-field gradient contrast microscopy using an infrared LED (850 nm, M850L2, Thorlabs, USA) as the light source. A low-magnification objective lens (UPlanSApp 4×/ NA 0.16, Olympus, Japan) was used to visualize and position the slices. A high-magnification water immersion lens (LUMPlanFLN 60×/ NA 1.00, Olympus, Japan) was used to identify neurons for whole-cell recordings.

Borosilicate glass (inner diameter 0.86 mm, outer diameter 1.5 mm with filament, Warner Instruments, USA) was pulled using a P-97 micropipette puller (Sutter Instrument, USA) into patch pipettes with a tip resistance of 2~4 MΩ. Neurons targeted for whole-cell recordings were obtained using micromanipulators (MP-225, ROE-200, MPC-200, Sutter Instrument, USA) and a patch-clamp amplifier (Multiclamp 700B, Axon Instruments, USA). Pipettes containing potassium-based or cesium-based internal solutions were used for voltage-clamp recordings (composition of the internal solution, in mM: 128 potassium or cesium methanesulfonate, 10 HEPES, 10 phosphocreatine, 4 MgCl₂, 4 ATP, 0.4 GTP, 3 ascorbate, 1 EGTA, 1 QX-314, and 0.05 Alexa Flour hydrazide, with 4 mg/ml biocytin, at 7.25 pH and 290–295 mOsm). All recordings were made in 34°C ACSF with the temperature controlled by an in-line feedback-controlled heater (TC 324B, Warner Instruments, USA). Recordings with series resistance > 40 MΩ were excluded.

A command potential of –70 mV was applied to isolate excitatory (glutamatergic) post synaptic currents (EPSCs). To test for input to a neuron, blue-laser illuminations (1 ms long pulses, 473 nm, ~ 2 mW, ~ 57 μm spot size; MLL-FN473, CNI Laser, China) were delivered onto a nearby spot of the Si mesh.

Multiple trials were sampled at an interstimulus interval of at least 30 s. Recorded currents were amplified, filtered at 4 kHz, and sampled at 40 kHz. Data were acquired using Ephys software⁵⁶ and analyzed using routines written in MATLAB (MathWorks, USA).

3) *In vivo* experiments with distributed Si meshes.

Wild-type mice (C57BL/6, female and male; Jackson Laboratory, USA) were used, at an age of 6–9 weeks old at the time of the *in vivo* experiments.

a) Pre-stimulation surgeries.—The mouse was deeply anesthetized with ketamine-xylazine (ketamine 80~100 mg/kg, xylazine 5~15 mg/kg, injected intraperitoneally) before the placement of the cranial mounting hardware. A small skin incision was first made over the cerebellum to expose the skull. A stainless-steel set screw (single-ended #8–32, SS8S050, Thorlabs, USA), crimped with a spade terminal (non-insulated, 69145K438, McMaster-Carr, USA) was then affixed with dental cement to the skull. This set screw was later screwed into a tapped hole located at the top of a 1/2" optical post for the head fixation.

After being head-fixed as described above, craniotomies were made over the motor and somatosensory cortices using a dental drill with large enough openings (~ 2.5 mm) to allow the attachment of a silicon mesh on the cortex and the passage of a linear probe. The dura was peeled for a full exposure of the cortex, which was important for a good signal transduction at the Si-brain interface. The mouse was then placed in the recording apparatus with the body temperature monitored with a rectal probe and maintained at ~ 37.0 °C via a feedback-controlled heating pad (FHC, Bowdoin, USA). During the subsequent recordings, ACSF was frequently applied to the exposed brain area to prevent the damage from dehydration. The level of anesthesia was continuously monitored based on whisker movements and paw-pinching/eye-blinking reflexes. Additional anesthetics with 50% of the induction dosage were given when required.

b) Photostimulation apparatus.—A customized laser scanning apparatus with a blue laser source (LY473III-100, wavelength 473 nm, maximum power ~ 100 mW, beam diameter ~2 mm) mounted on a 3D linear stage was positioned above the mouse head. In the apparatus, the laser beam from the light source goes through an acousto-optic modulator (AOM) and an iris before being deflected by a pair of galvanometer scanners and focused to the Si mesh by a plano-convex spherical lens.

The output laser power was controlled using a customized AOM driver modulated by signal waveforms delivered via a commercial multifunction (analog and digital) interface board (NI USB 6229, National Instruments, USA). A short pulse train was also sent to digitally encode the parameters of the light waveform such as the start point through the digital input port of the electrophysiology data acquisition (DAQ) board. Software tools (LabVIEW, National Instruments, USA) including a graphical user interface (GUI, GenWave) were developed to generate and transfer waveforms to the AOM driver. The system was calibrated using a power meter to determine the relationship between the driver input voltage and the laser scanner output power.

c) Electrophysiology apparatus.—Silicon probes of 32-channel linear microelectrode arrays with ~1 M Ω impedances and 50- μ m spacings (model A1 32–6mm-50–177, NeuroNexus, USA) were used for electrophysiological recordings. The probe was fixed to a motorized 4-axis micromanipulator, assembled by mounting a MTSA1 linear translator (Thorlabs, USA) onto a MP285 3-axis manipulator (Sutter Instrument, USA), and positioned

under stereoscopic visualizations over a distributed silicon mesh which has been attached to the cortical surface (with the Si layer facing towards the tissue). The probe was tilted by $\sim 30^\circ$ off the vertical axis for a better collection of the neural signals under the silicon mesh. The probe was then slowly inserted into the cortex at a rate of $2 \mu\text{m/s}$ controlled by LabVIEW, until it reached a depth of $1600 \mu\text{m}$ from the pia, with the entry point in the sensorimotor cortex adjacent to the edge of the silicon mesh. Laser pulses with various powers (up to 5 mW , $\sim 216 \mu\text{m}$ spot size) and durations (up to 100 ms) were delivered onto the Si mesh for the photostimulation of the brain.

Signals were amplified using a RHD2132 amplifier board based on a RHD2132 digital electrophysiology interface chip (Intan Technologies, USA). The filter was set to an analog bandpass of $0.1 \sim 7.5 \text{ kHz}$ with a digital filter cutoff of 1 Hz . The single channel sample rate was set to 30K SPS .

For hardware control, we used a RHD2000 USB Interface Board (Intan Technologies, USA) for the communication with other digital devices and the streaming of all the neural-signal data from the RHD2000 amplifiers. The USB port of the module was linked with a USB cable to pipe the data stream in to and out of the computer. In this experiment, the digital ports included in the DAQ board were only used for the acquisition of the photostimulation parameters from the AOM controller.

C++/Qt based experimental interface software (Intan Technologies, USA) was used for the amplifier configuration, online visualization, and data logging.

d) Forelimb movement study apparatus.—A Chameleon3 USB3 CMOS Mono camera (CM3-U3-13Y3M-CS, FLIR Systems, USA) configured at 640×512 pixels (2×2 binning) was used to record the body movements following the laser stimulations. The video recording was triggered and synchronized by the laser scanning control board with the frame rate of 100 Hz . 50 frames were collected before the start of the stimulation and a total of 100 frames were recorded for a full trial. A fixed focal length lens (35 mm EFL , $f/2.0$, Navitar, USA) was mounted on the camera for the focusing. The centroids of the mouse claws were tracked in each frame to investigate the forelimb movements following the laser stimulations. The trajectories of the centroids were quantified to illustrate the movements in each trial.

e) Data analyses.—The recorded data were stored as raw signals from the amplifiers and filtered by a 60 Hz notch filter. To reduce the contaminations of the probe recording signals due to the strong photovoltaic effect of the Si mesh, we used a digital high-pass filter (800 Hz cut-off, 2nd-order Butterworth), to shrink the photovoltaic artifact to the first 3 ms post-stimulus window.

The following routines were performed to further analyze the data. First of all, a threshold detector was applied, with the threshold set to the 5 times of the standard deviation (5 SD) to detect the spikes. To mask the photovoltaic effect, spike counts of the first 3 ms window were then replaced by null values. Finally, neural response time stamps were determined for each detected spike and the response waveforms were plotted from -0.67 ms to 1.33 ms with

respect to the detected spike time stamp, *i.e.*, 20 points before and 40 points after the spike time stamp with a sampling rate of 30 kHz. The detected waveforms were sorted according to the similarity of the shapes, *i.e.*, peak to valley amplitudes of the responses. All the analysis codes were written in Matlab (Mathworks, USA).

The time stamps of all the spikes from each channel were used to generate the peristimulus time histogram and the heat maps, which represent the instantaneous firing rate, with 1-ms binning. Responses were averaged across all trials in each channel to yield a mean histogram.

Micro computed tomography (microCT) of the Si/brain interface.—MicroCT images of gold-decorated Si meshes attached to dead mouse brains were performed on the XCUBE (Molecubes NV., Belgium) by the Integrated Small Animal Imaging Research Resource (iSAIRR) at the University of Chicago. Images were acquired with an x-ray source of 50 kVp and 200 μ A in a single frame of 960 projections. Volumetric CT images were reconstructed in a $400 \times 400 \times 400$ format with voxel dimensions of $100 \mu\text{m}^3$. Images were analyzed using AMIRA 5.6 (Thermo Fisher Scientific, USA).

Device-brain peeling adhesion test.—Adult C57BL/6 mice (Jackson Laboratory, USA) were sacrificed shortly before the mechanical test. Mouse brains were harvested from dead animals and placed inside PBS solutions prior to the adhesion tests by a tensile test machine (Zwick-Roell, Germany, zwickiLine Z0.5). Briefly, the brain was fixed on a glass slide using a tissue adhesive (Ted Pella, USA, Pelco Pro CA44) and the device was held tightly by a grip. After forming a conformal contact between the device and the brain cortex with an area of $\sim 8 \text{ mm} \times 4 \text{ mm}$, a unidirectional tension was applied to peel the device off the brain while the force and the extension were recorded simultaneously. The loading rate was kept constant at 3 mm/min. The adhesion energy per area was calculated by the integration of the force-extension curves divided by the contact areas.

Analysis of the photo-response measurements.

In a typical photo-response measurement, a glass micropipette, with the potential holding at a fixed level (V_p), was positioned near a Si material surface immersed in PBS, and a 10-ms long light pulse was delivered to the material in the middle of the trial. Therefore, the recorded current across the pipette tip can be divided into two parts, namely the baseline current I_0 at the dark stage and the time-dependent light-generated current $I_{\text{light}}(t)$ at the light stage. During the light illumination period, two parallel processes originated from the Si material can contribute to $I_{\text{light}}(t)$.

The first one is the photoelectric process where the light-generated excessive carriers will accumulate on the Si surface and change the local surface potential. Ions in the nearby medium will be attracted/repelled with respect to this photo-generated potential and create the ionic currents. Since the variation of the surface potential is only a function of the carrier dynamics on the Si surface, the photoelectrically-induced ionic current ($I_{\text{electric}}(t)$) is therefore independent of the holding current level I_0 .

Another process is related to the photothermal effect of Si where the recombination of light-generated carriers converts part of the input photon energy into the vibrational energy of the Si lattice, which dissipates heat through both Si and the surrounding electrolyte. For the electrolyte with an elevated temperature, mobilities of the ions will increase, resulting in a reduced pipette tip resistance R . Even under a fixed holding potential V_p , the current during the light illumination period will change due to the decrease of the pipette resistance. Therefore, the thermally-induced current ($I_{\text{thermal}}(t)$), is strongly related to the holding potential V_p and the baseline current I_0 , where $V_p = I_0 \times R_0$, R_0 is the pipette resistance in dark.

Given the significantly different dependences on the holding current I_0 for the electrically- ($I_{\text{electric}}(t)$) and thermally-induced currents ($I_{\text{thermal}}(t)$), the total light-generated currents ($I_{\text{light}}(t) = I_{\text{electric}}(t) + I_{\text{thermal}}(t)$) can be potentially decoupled by analyzing current traces recorded at different holding levels.

At a given time point t during the light illumination period, the recorded current, $I_0 + I_{\text{light}}(t)$, excluding the photoelectrically-induced current part $I_{\text{electric}}(t)$, and the pipette tip resistance $R(t)$ follow the Ohm's law as long as the holding potential V_p is fixed.

$$V_p = I_0 \times R_0 = (I_0 + \Delta I_{\text{light}}(t) - \Delta I_{\text{electric}}(t)) \times R(t). \quad (1)$$

Rearranging Eq. 1 gives the relationship between the light-induced current $I_{\text{light}}(t)$ and the holding current I_0 that

$$\Delta I_{\text{light}}(t) = \left(\frac{R_0}{R(t)} - 1 \right) \times I_0 + \Delta I_{\text{electric}}(t). \quad (2)$$

As shown in Eq. 2, the photoelectric effect is explicitly manifested as the intercept of the curve. A photocurrent plot can be generated by plotting the fitted intercept values over time as shown in Fig. 2 and Supplementary Figs. 9, 11, and 14. Two types of photoelectric responses, *i.e.*, capacitive and Faradaic, are further identified based on the dynamics and the amplitude of the currents. Two spiky features at the onset and offset of the light illumination are capacitive currents corresponding to the capacitive charging/discharging processes at the Si/electrolyte interface. A long-lasting current with a lower amplitude is the Faradaic current due to the surface redox reactions.

The photothermal effect, on the other hand, is implicitly embedded in the fitted slope as the pipette resistance is a function of temperature. To calculate the photothermally-induced temperature change of the surrounding medium, a calibration curve of the pipette resistance over temperature is needed, which typically follows an Arrhenius-type relationship⁵⁷ that

$$\ln R = a \times \frac{1}{T} + c, \quad (3)$$

where a and c represent the slope and intercept values.

In conjunction with the slope $k(t)$ from the $I_{\text{light}}(t) - I_0$ plot that

$$R(t) = \frac{R_0}{k(t) + 1}, \quad (4)$$

the final temperature of the surround medium heated from the photothermal effect is determined only by the slopes of the $I_{\text{light}}(t) - I_0$ and the $\ln R - 1/T$ curves that

$$T(t) = \frac{1}{\frac{1}{T_0} - \frac{1}{a} \ln(k(t) + 1)}. \quad (5)$$

Notably, since the photothermal effect is a function of the illumination duration, the slope of the $I_{\text{light}}(t) - I_0$ plot is also time dependent. The maximal temperature is reached after 10 ms of illumination so $I_{\text{light},10 \text{ ms}} - I_0$ plots were used to assess the photothermal responses of various Si materials presented in Fig. 2, Table 1, and Supplementary Figs. 9, 11, 13, and 14. A temperature over time curve can also be generated using the fitted slope values from each time point as shown in Fig. 2.

In summary, the $I_{\text{light},10 \text{ ms}} - I_0$ plot method can be applied to ***virtually all kinds of materials other than just Si*** to assess their photo-responses, which will fall into the following four categories.

1) In one extreme case where the material has only the photothermal effect without any photoelectric effect, *i.e.*, $I_{\text{electric}} = 0$ at all time, Eq. 2 will be reduced to

$$\Delta I_{\text{light}, 10 \text{ ms}} = \left(\frac{R_0}{R_{10 \text{ ms}}} - 1 \right) \times I_0. \quad (6)$$

The $I_{\text{light},10 \text{ ms}} - I_0$ plot will be a slanted line with a zero intercept.

2) In another extreme scenario where the material has only the photoelectric effect without any photothermal effect, *i.e.*, $R_0 = R_{10 \text{ ms}}$, Eq. 2 can be written as

$$\Delta I_{\text{light}, 10 \text{ ms}} = \Delta I_{\text{electric}, 10 \text{ ms}}. \quad (7)$$

The $I_{\text{light},10 \text{ ms}} - I_0$ plot will be a horizontal line with a non-zero intercept.

3) If a material does not have any photo-responses, Eq. 2 will be

$$\Delta I_{\text{light}, 10 \text{ ms}} = 0. \quad (8)$$

The $I_{\text{light},10\text{ ms}} - I_0$ plot will be a horizontal line with a zero intercept.

4) In any intermediate situations where both the photoelectric and the photothermal effects coexist, the original form of Eq. 2 applies that

$$\Delta I_{\text{light},10\text{ ms}} = \left(\frac{R_0}{R_{10\text{ ms}}} - 1 \right) \times I_0 + \Delta I_{\text{electric},10\text{ ms}} \quad (9)$$

The $I_{\text{light},10\text{ ms}} - I_0$ plot will be a slanted line with a non-zero intercept.

Supplementary Material

Refer to Web version on PubMed Central for supplementary material.

Acknowledgements

This work is supported by the Air Force Office of Scientific Research (AFOSR FA9550-14-1-0175, FA9550-15-1-0285), the National Science Foundation (NSF CAREER, DMR-1254637; NSF MRSEC, DMR 1420709), the Searle Scholars Foundation, the National Institutes of Health (NIH NS101488, and NS061963). This work made use of the JEOL JEM-ARM200CF and JEOL JEM-3010 TEM in the Electron Microscopy Service (Research Resources Center, UIC). The acquisition of the UIC JEOL JEM-ARM200CF was supported by a MRI-R2 grant from the National Science Foundation (DMR-0959470). The animal imaging work conducted at the Integrated Small Animal Imaging Research Resource (iSAIRR) at the University of Chicago was supported in part by funding provided by the Virginia and D. K. Ludwig Fund for Cancer Research via the Imaging Research Institute in the Biological Sciences Division, by the University of Chicago Comprehensive Cancer Center including an NIH grant P30 CA14599, and by the Department of Radiology. Part of the schematic in Fig. 4c was generated from a 3D anatomy software purchased from biosphera.org. The authors thank L. Yu, V. Sharapov, S. Patel, Y. Chen, Q. Guo, and J. Jureller for providing technical supports.

References:

1. Viventi J, Kim DH, Vigeland L, Frechette ES, Blanco JA, Kim YS, Avrin AE, Tiruvadi VR, Hwang SW, Vanleer AC, Wulsin DF, Davis K, Gelber CE, Palmer L, Van der Spiegel J, Wu J, Xiao J, Huang Y, Contreras D, Rogers JA & Litt B Flexible, foldable, actively multiplexed, high-density electrode array for mapping brain activity in vivo. *Nature Neuroscience* 14, 1599–1605, 10.1038/nn.2973 (2011). [PubMed: 22081157]
2. Tian B, Cohen-Karni T, Qing Q, Duan X, Xie P & Lieber CM Three-dimensional, flexible nanoscale field-effect transistors as localized bioprobes. *Science* 329, 830–834, 10.1126/science.1192033 (2010). [PubMed: 20705858]
3. Liu J, Fu TM, Cheng Z, Hong G, Zhou T, Jin L, Duvvuri M, Jiang Z, Kruskal P, Xie C, Suo Z, Fang Y & Lieber CM Syringe-injectable electronics. *Nature Nanotechnology* 10, 629–636, 10.1038/nnano.2015.115 (2015).
4. Chiappini C, De Rosa E, Martinez JO, Liu X, Steele J, Stevens MM & Tasciotti E Biodegradable silicon nanoneedles delivering nucleic acids intracellularly induce localized in vivo neovascularization. *Nature Materials* 14, 532–539, 10.1038/nmat4249 (2015). [PubMed: 25822693]
5. Tian B, Liu J, Dvir T, Jin L, Tsui JH, Qing Q, Suo Z, Langer R, Kohane DS & Lieber CM Macroporous nanowire nanoelectronic scaffolds for synthetic tissues. *Nature Materials* 11, 986–994, 10.1038/nmat3404 (2012). [PubMed: 22922448]
6. Fang H, Yu KJ, Gloschat C, Yang Z, Chiang CH, Zhao J, Won SM, Xu S, Trumpis M, Zhong Y, Song E, Han SW, Xue Y, Xu D, Cauwenberghs G, Kay M, Huang Y, Viventi J, Efimov IR & Rogers JA Capacitively coupled arrays of multiplexed flexible silicon transistors for long-term cardiac electrophysiology. *Nature Biomedical Engineering* 1, 0038, 10.1038/s41551-017-0038 (2017).

7. Colicos MA, Collins BE, Sailor MJ & Goda Y Remodeling of synaptic actin induced by photoconductive stimulation. *Cell* 107, 605–616 (2001). [PubMed: 11733060]
8. Tee BC, Chortos A, Berndt A, Nguyen AK, Tom A, McGuire A, Lin ZC, Tien K, Bae WG, Wang H, Mei P, Chou HH, Cui B, Deisseroth K, Ng TN & Bao Z A skin-inspired organic digital mechanoreceptor. *Science* 350, 313–316, 10.1126/science.aaa9306 (2015). [PubMed: 26472906]
9. Khodagholy D, Gelineas JN, Thesen T, Doyle W, Devinsky O, Malliaras GG & Buzsaki G NeuroGrid: recording action potentials from the surface of the brain. *Nature Neuroscience* 18, 310–315, 10.1038/nn.3905 (2015). [PubMed: 25531570]
10. Fu TM, Hong G, Zhou T, Schuhmann TG, Viveros RD & Lieber CM Stable long-term chronic brain mapping at the single-neuron level. *Nature Methods* 13, 875–882, 10.1038/nmeth.3969 (2016). [PubMed: 27571550]
11. Chortos A, Liu J & Bao Z Pursuing prosthetic electronic skin. *Nature Materials* 15, 937–950, 10.1038/nmat4671 (2016). [PubMed: 27376685]
12. Someya T, Bao Z & Malliaras GG The rise of plastic bioelectronics. *Nature* 540, 379–385, 10.1038/nature21004 (2016). [PubMed: 27974769]
13. Chiappini C, Martinez JO, De Rosa E, Almeida CS, Tasciotti E & Stevens MM Biodegradable nanoneedles for localized delivery of nanoparticles in vivo: exploring the biointerface. *ACS Nano* 9, 5500–5509, 10.1021/acsnano.5b01490 (2015). [PubMed: 25858596]
14. Zimmerman JF, Murray GF, Wang Y, Jumper JM, Austin JR, II & Tian B Free-standing kinked silicon nanowires for probing inter- and intracellular force dynamics. *Nano Letters* 15, 5492–5498, 10.1021/acs.nanolett.5b01963 (2015). [PubMed: 26192816]
15. Chu B, Burnett W, Chung JW & Bao Z Bring on the bodyNET. *Nature* 549, 328–330, 10.1038/549328a (2017). [PubMed: 28933443]
16. Sakimoto KK, Wong AB & Yang P Self-photosensitization of nonphotosynthetic bacteria for solar-to-chemical production. *Science* 351, 74–77, 10.1126/science.aad3317 (2016). [PubMed: 26721997]
17. Liu C, Colon BC, Ziesack M, Silver PA & Nocera DG Water splitting-biosynthetic system with CO₂ reduction efficiencies exceeding photosynthesis. *Science* 352, 1210–1213, 10.1126/science.aaf5039 (2016). [PubMed: 27257255]
18. Chen R, Romero G, Christiansen MG, Mohr A & Anikeeva P Wireless magnetothermal deep brain stimulation. *Science* 347, 1477–1480, 10.1126/science.1261821 (2015). [PubMed: 25765068]
19. Seo D, Neely RM, Shen K, Singhal U, Alon E, Rabaey JM, Carmena JM & Maharbiz MM Wireless recording in the peripheral nervous system with ultrasonic neural dust. *Neuron* 91, 529–539, 10.1016/j.neuron.2016.06.034 (2016). [PubMed: 27497221]
20. Nadeau P, El-Damak D, Glettig D, Kong YL, Mo S, Cleveland C, Booth L, Roxhed N, Langer R, Chandrakasan AP & Traverso G Prolonged energy harvesting for ingestible devices. *Nature Biomedical Engineering* 1, 0022, 10.1038/s41551-016-0022 (2017).
21. Jiang Y, Carvalho-de-Souza JL, Wong RC, Luo Z, Isheim D, Zuo X, Nicholls AW, Jung IW, Yue J, Liu DJ, Wang Y, De Andrade V, Xiao X, Navrazhnykh L, Weiss DE, Wu X, Seidman DN, Bezanilla F & Tian B Heterogeneous silicon mesostructures for lipid-supported bioelectric interfaces. *Nature Materials* 15, 1023–1030, 10.1038/nmat4673 (2016). [PubMed: 27348576]
22. Grossman N, Bono D, Dedic N, Kodandaramaiah SB, Rudenko A, Suk HJ, Cassara AM, Neufeld E, Kuster N, Tsai LH, Pascual-Leone A & Boyden ES Noninvasive deep brain stimulation via temporally interfering electric fields. *Cell* 169, 1029–1041 10.1016/j.cell.2017.05.024 (2017). [PubMed: 28575667]
23. Dagdeviren C, Javid F, Joe P, von Erlach T, Bense T, Wei Z, Saxton S, Cleveland C, Booth L, McDonnell S, Collins J, Hayward A, Langer R & Traverso G Flexible piezoelectric devices for gastrointestinal motility sensing. *Nature Biomedical Engineering* 1, 807–817, 10.1038/s41551-017-0140-7 (2017).
24. Zimmerman JF, Parameswaran R, Murray G, Wang Y, Burke M & Tian B Cellular uptake and dynamics of unlabeled freestanding silicon nanowires. *Science Advances* 2, e1601039, 10.1126/sciadv.1601039 (2016). [PubMed: 28028534]

25. Dalby MJ, Gadegaard N & Oreffo RO Harnessing nanotopography and integrin-matrix interactions to influence stem cell fate. *Nature Materials* 13, 558–569, 10.1038/nmat3980 (2014). [PubMed: 24845995]
26. Tian B, Zheng X, Kempa TJ, Fang Y, Yu N, Yu G, Huang J & Lieber CM Coaxial silicon nanowires as solar cells and nanoelectronic power sources. *Nature* 449, 885–889, 10.1038/nature06181 (2007). [PubMed: 17943126]
27. Ghezzi D, Antognazza MR, Maccarone R, Bellani S, Lanzarini E, Martino N, Mete M, Pertile G, Bisti S, Lanzani G & Benfenati F A polymer optoelectronic interface restores light sensitivity in blind rat retinas. *Nature Photonics* 7, 400–406, 10.1038/nphoton.2013.34 (2013). [PubMed: 27158258]
28. Walter MG, Warren EL, McKone JR, Boettcher SW, Mi Q, Santori EA & Lewis NS Solar water splitting cells. *Chemical Reviews (Washington, DC, United States)* 110, 6446–6473, 10.1021/cr1002326 (2010).
29. Kang D, Kim TW, Kubota SR, Cardiel AC, Cha HG & Choi KS Electrochemical Synthesis of Photoelectrodes and Catalysts for Use in Solar Water Splitting. *Chemical Reviews (Washington, DC, United States)* 115, 12839–12887, 10.1021/acs.chemrev.5b00498 (2015).
30. Merrill DR, Bikson M & Jefferys JG Electrical stimulation of excitable tissue: design of efficacious and safe protocols. *Journal of Neuroscience Methods* 141, 171–198, 10.1016/j.jneumeth.2004.10.020 (2005). [PubMed: 15661300]
31. Ziegenfuss JS, Biswas R, Avery MA, Hong K, Sheehan AE, Yeung YG, Stanley ER & Freeman MR Draper-dependent glial phagocytic activity is mediated by Src and Syk family kinase signalling. *Nature* 453, 935–939, 10.1038/nature06901 (2008). [PubMed: 18432193]
32. Yoon J, Park J, Choi M, Choi WJ & Choi C Application of femtosecond-pulsed lasers for direct optical manipulation of biological functions. *Annalen Der Physik* 525, 205–214, 10.1002/andp.201200099 (2013).
33. White JA, Blackmore PF, Schoenbach KH & Beebe SJ Stimulation of capacitative calcium entry in HL-60 cells by nanosecond pulsed electric fields. *Journal of Biological Chemistry* 279, 22964–22972, 10.1074/jbc.M311135200 (2004). [PubMed: 15026420]
34. Hua W, Young EC, Fleming ML & Gelles J Coupling of kinesin steps to ATP hydrolysis. *Nature* 388, 390–393, 10.1038/41118 (1997). [PubMed: 9237758]
35. Stout CE, Costantin JL, Naus CC & Charles AC Intercellular calcium signaling in astrocytes via ATP release through connexin hemichannels. *Journal of Biological Chemistry* 277, 10482–10488, 10.1074/jbc.M109902200 (2002). [PubMed: 11790776]
36. Guthrie PB, Knappenberger J, Segal M, Bennett MV, Charles AC & Kater SB ATP released from astrocytes mediates glial calcium waves. *Journal of Neuroscience* 19, 520–528 (1999). [PubMed: 9880572]
37. Chen HX & Diebold G Chemical generation of acoustic waves: A giant photoacoustic effect. *Science* 270, 963–966, 10.1126/science.270.5238.963 (1995).
38. Tang-Schomer MD, Patel AR, Baas PW & Smith DH Mechanical breaking of microtubules in axons during dynamic stretch injury underlies delayed elasticity, microtubule disassembly, and axon degeneration. *FASEB Journal* 24, 1401–1410, 10.1096/fj.09-142844 (2010). [PubMed: 20019243]
39. Maya-Vetencourt JF, Ghezzi D, Antognazza MR, Colombo E, Mete M, Feyen P, Desii A, Buschiazzi A, Di Paolo M, Di Marco S, Ticconi F, Emionite L, Shmal D, Marini C, Donelli I, Freddi G, Maccarone R, Bisti S, Sambuceti G, Pertile G, Lanzani G & Benfenati F A fully organic retinal prosthesis restores vision in a rat model of degenerative blindness. *Nature Materials* 16, 681–689, 10.1038/nmat4874 (2017). [PubMed: 28250420]
40. Ghezzi D, Antognazza MR, Dal Maschio M, Lanzarini E, Benfenati F & Lanzani G A hybrid bioorganic interface for neuronal photoactivation. *Nature Communications* 2, 166, 10.1038/ncomms1164 (2011).
41. Lorach H, Goetz G, Smith R, Lei X, Mandel Y, Kamins T, Mathieson K, Huie P, Harris J, Sher A & Palanker D Photovoltaic restoration of sight with high visual acuity. *Nature Medicine* 21, 476–482, 10.1038/nm.3851 (2015).

42. Katz LC & Dalva MB Scanning laser photostimulation: a new approach for analyzing brain circuits. *Journal of Neuroscience Methods* 54, 205–218 (1994). [PubMed: 7869753]
43. Yamawaki N, Suter BA, Wickersham IR & Shepherd GM Combining optogenetics and electrophysiology to analyze projection neuron circuits. *Cold Spring Harbor Protocols* 2016, doi: 10.1101/pdb.prot090084 doi:10.1101/pdb.prot090084.10.1101/pdb.prot090084 doi: 10.1101/pdb.prot090084 (2016).
44. Paralikar KJ, Rao CR & Clement RS New approaches to eliminating common-noise artifacts in recordings from intracortical microelectrode arrays: inter-electrode correlation and virtual referencing. *Journal of Neuroscience Methods* 181, 27–35, 10.1016/j.jneumeth.2009.04.014 (2009). [PubMed: 19394363]
45. Veerabhadrapa R, Lim CP, Nguyen TT, Berk M, Tye SJ, Monaghan P, Nahavandi S & Bhatti A Unified selective sorting approach to analyse multi-electrode extracellular data. *Scientific Reports* 6, 28533, 10.1038/srep28533 (2016). [PubMed: 27339770]
46. Rossant C, Kadir SN, Goodman DFM, Schulman J, Hunter MLD, Saleem AB, Grosmark A, Belluscio M, Denfield GH, Ecker AS, Tolias AS, Solomon S, Buzsaki G, Carandini M & Harris KD Spike sorting for large, dense electrode arrays. *Nature Neuroscience* 19, 634–641, 10.1038/nn.4268 (2016). [PubMed: 26974951]
47. Yamawaki N, Borges K, Suter BA, Harris KD & Shepherd GM A genuine layer 4 in motor cortex with prototypical synaptic circuit connectivity. *Elife* 3, e05422, 10.7554/eLife.05422 (2014). [PubMed: 25525751]
48. Li X, Yamawaki N, Barrett JM, Kording KP & Shepherd GMG Corticocortical signaling drives activity in a downstream area rapidly and scalably. *bioRxiv*, doi: 10.1101/154914 , doi: 10.1101/154914.10.1101/154914, doi: 10.1101/154914 (2017).
49. Tennant KA, Adkins DL, Donlan NA, Asay AL, Thomas N, Kleim JA & Jones TA The organization of the forelimb representation of the C57BL/6 mouse motor cortex as defined by intracortical microstimulation and cytoarchitecture. *Cerebral Cortex* 21, 865–876, 10.1093/cercor/bhq159 (2011). [PubMed: 20739477]
50. Boyden ES, Zhang F, Bamberg E, Nagel G & Deisseroth K Millisecond-timescale, genetically targeted optical control of neural activity. *Nature Neuroscience* 8, 1263–1268, 10.1038/nn1525 (2005). [PubMed: 16116447]
51. Dai J, Brooks DI & Sheinberg DL Optogenetic and electrical microstimulation systematically bias visuospatial choice in primates. *Current Biology* 24, 63–69, 10.1016/j.cub.2013.11.011 (2014). [PubMed: 24332543]
52. Stauffer WR, Lak A, Yang A, Borel M, Paulsen O, Boyden ES & Schultz W Dopamine neuron-specific optogenetic stimulation in Rhesus Macaques. *Cell* 166, 1564–1571 10.1016/j.cell.2016.08.024 (2016). [PubMed: 27610576]
53. Chen R, Canales A & Anikeeva P Neural recording and modulation technologies. *Nature Reviews Materials* 2, 10.1038/natrevmats.2016.93 (2017).
54. Voyles PM, Grazul JL & Muller DA Imaging individual atoms inside crystals with ADF-STEM. *Ultramicroscopy* 96, 251–273, 10.1016/S0304-3991(03)00092-5 (2003). [PubMed: 12871793]
55. Voyles PM, Muller DA, Grazul JL, Citrin PH & Gossmann HJ Atomic-scale imaging of individual dopant atoms and clusters in highly n-type bulk Si. *Nature* 416, 826–829, 10.1038/416826a (2002). [PubMed: 11976677]
56. Suter BA, O'Connor T, Iyer V, Petreanu LT, Hooks BM, Kiritani T, Svoboda K & Shepherd GM Ephus: multipurpose data acquisition software for neuroscience experiments. *Frontiers in Neural Circuits* 4, 100, 10.3389/fncir.2010.00100 (2010). [PubMed: 21960959]
57. Yao J, Liu B & Qin F Rapid temperature jump by infrared diode laser irradiation for patch-clamp studies. *Biophysical Journal* 96, 3611–3619, 10.1016/j.bpj.2009.02.016 (2009). [PubMed: 19413966]

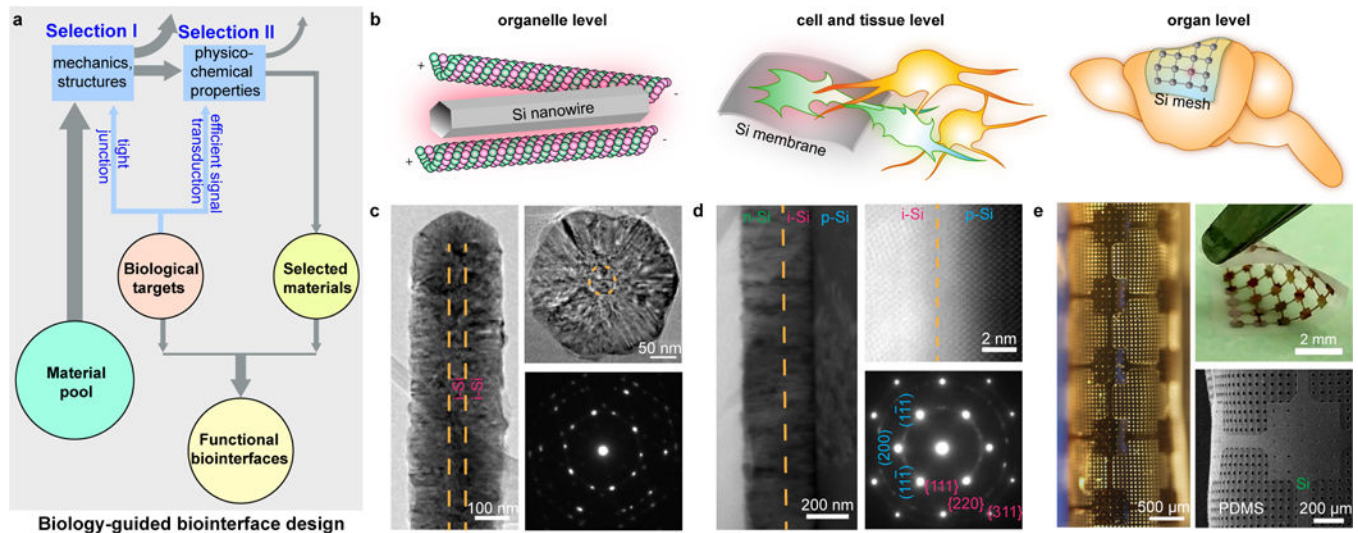


Figure 1 | Si structures for multiscale biointerfaces.

a, A schematic diagram illustrating the principle of biology-guided biointerface design. The intended biological targets place selection criteria for material structure (I) and function (II), so that the selected materials would display a better chance to establish functional biointerfaces. **b**, Silicon-based materials, *e.g.*, nanowires (left), thin membranes (middle), and distributed meshes (right), are chosen after **Selection I** to form tight interfaces with various biological targets, spanning multiple length scales, *e.g.*, organelles (left), single cells or small tissues (middle), and organs (right). **c**, An intrinsic-intrinsic coaxial Si nanowire is synthesized from the deposition of a thick shell over a thin VLS-grown nanowire backbone as shown in a side-view TEM image (left). A cross-sectional TEM image (upper right) shows diameters of ~ 50 nm and ~ 270 nm for the core and shell, respectively. A corresponding SAED pattern (lower right) confirms the nanocrystalline structure. Orange dashed lines highlight the core/shell boundaries. **d**, A multilayered *p-i-n* Si diode junction made by a CVD synthesis of intrinsic (magenta) and *n*-type (green) Si layers onto a *p*-type (cyan) Si SOI substrate. A cross-sectional TEM image (left) shows the columnar structures of the intrinsic and *n*-type layers. A low-angle annular dark field scanning TEM (LAADF STEM) image (upper right) and a SAED (zone axis $B = [011]$, lower right) pattern taken at the *p*-type (cyan)/intrinsic (magenta) interface both highlight the single crystalline *p*-type layer (isolated spots (blue) from SAED, periodic atomic columns from STEM) and the nanocrystalline intrinsic layer (concentric rings (magenta) from SAED, small crystal domains from STEM). A sharp and oxide free interface is evident from the STEM image with a junction width of < 1 nm. Orange dashed lines mark the intrinsic/*n*-type (left) and the *p*-type/intrinsic (upper right) interfaces. **e**, A flexible device composed of a stack of a distributed Si mesh and a holey PDMS membrane. The flexibility is demonstrated by optical (left) and scanning electron (lower right) micrographs and a photograph (upper right) taken from the same device under rolling or bending.

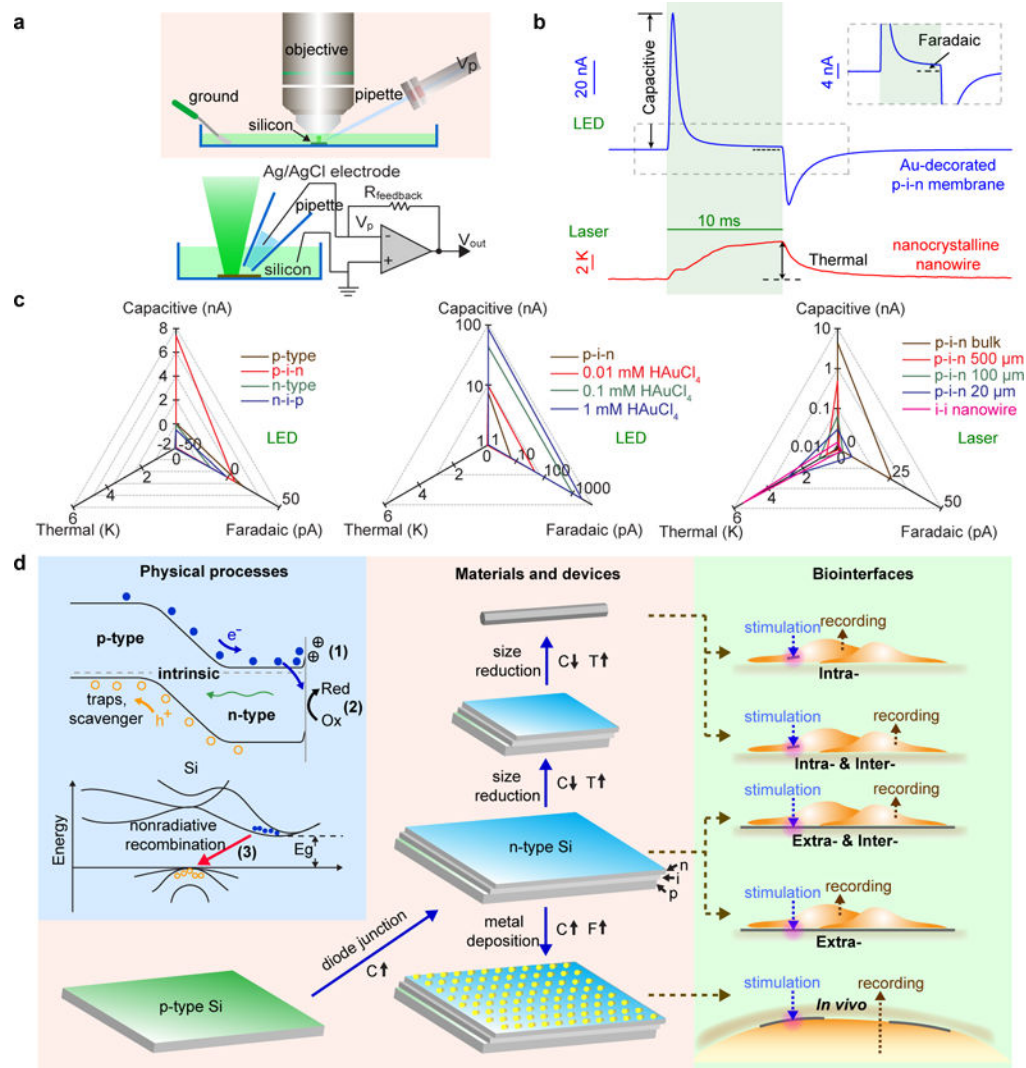


Figure 2 | Photo-responses of Si materials.

a, Schematic diagrams illustrating the experimental setup for the photo-response measurements from Si structures. Light pulses (530 nm LED or 532 nm laser) are delivered through a water-immersion objective to the Si submerged in a PBS solution. Light-induced currents are recorded at different pipette command potentials (V_p) using a voltage-clamp mode, from which capacitive, Faradaic and thermal components can be either directly measured or derived by mathematic fitting. **b**, Representative photo-responses of an Au-decorated *p-i-n* Si diode junction (top, from 1 mM HAuCl₄, LED illumination, ~ 12.05 mW, ~ 500 μm spot size, ~ 6 W/cm²) and an *i-i* nanocrystalline nanowire (bottom, laser illumination, 47.1 mW, ~ 5 μm spot size, ~ 240 kW/cm²) showing three major types of the responses, *i.e.*, capacitive (upper), Faradaic (upper inset), and thermal (lower). LED-induced capacitive and Faradaic currents are pronounced in the Au-decorated diode junction. The capacitive current is defined as the maximal current amplitude reached after the light onset while the Faradaic current is defined as the current amplitude at the time point of 8.5 ms since illumination starts. The nanocrystalline nanowire generate significant heating of the surrounding PBS via its photothermal effect under laser illumination. Green shaded areas

highlight the light illumination periods. The grey dashed box marks the region for the inset. **c**, Quantitative matrices of the three photo-responses, used to evaluate the impact of important materials parameters, *e.g.*, doping (left), surface chemistry (middle), and size (right). Diode junctions (left, *p-i-n* and *n-i-p*) show significantly enhanced capacitive currents versus uniformly doped SOI substrates (*p*-type and *n*-type). Au-decorated *p-i-n* diode junctions (middle) promote both capacitive and Faradaic currents. Si structures with smaller dimensions (right) show stronger photothermal responses. **d**, A principle for **Selection II** (Fig. 1a), highlighting the physical origins (light blue block), the material developing pathways (light orange block), and the projected biointerfaces (light green block). Fundamental processes include the accumulation of ions to balance light-generated excessive carriers near Si surface (**1**, capacitive, **C**), the metal-mediated redox reactions (**2**, Faradaic, **F**), and the thermalization through phonon emission (**3**, thermal, **T**). Considering the size and mechanics match at the biointerfaces (*i.e.*, **Selection I**, Fig. 1a), these Si structures can be utilized to form optically-controlled intra- (Si nanowires), inter- (Si nanowires and *p-i-n* diode junctions), and extra-cellular (pristine and metal-decorated *p-i-n* diode junctions) biointerfaces.

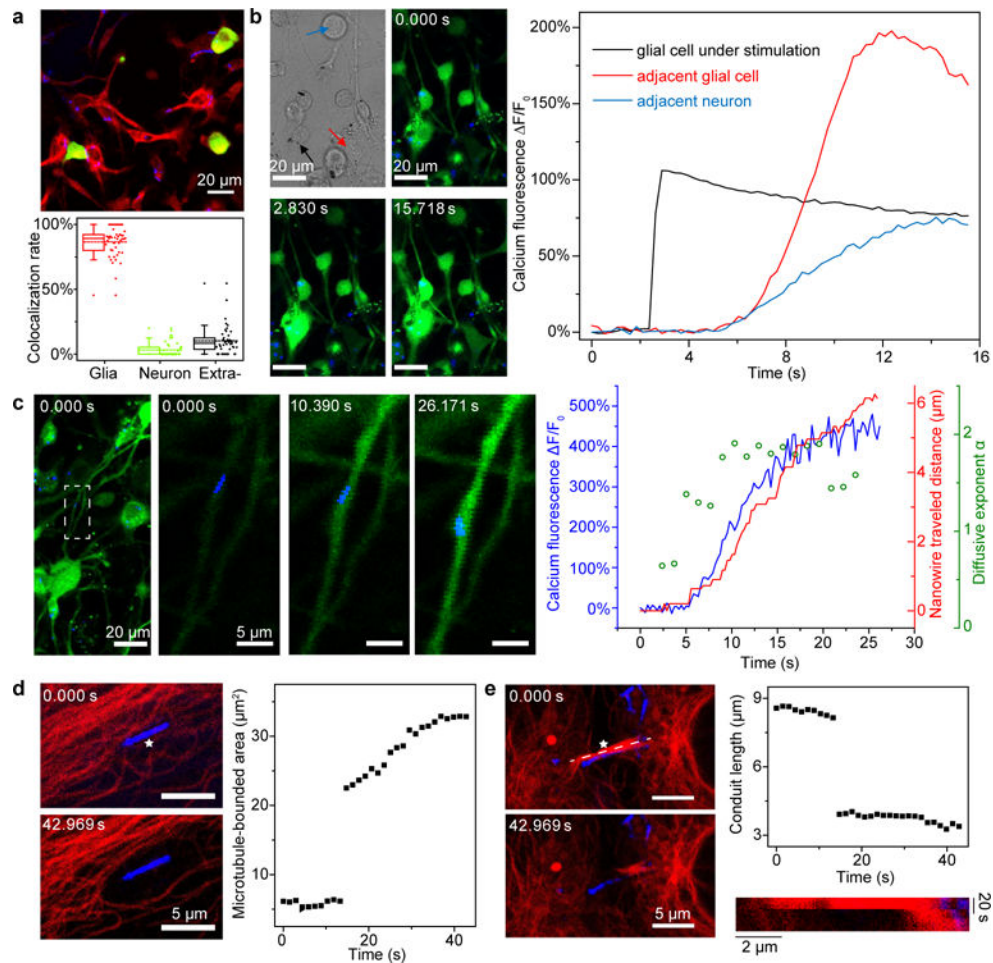


Figure 3 | Si nanowire-enabled intracellular stimulation interfaces.

a, A confocal microscope image (top) of a DRG-nanowire coculture shows the cell-type-specific overlapping of Si nanowires (green, neurons; red, glial cells; blue, Si nanowires). Statistical analysis of the nanowire-cell colocalization rate (bottom) reveals that $\sim 87\%$ of total nanowires overlap with glial cells, $\sim 3\%$ with neurons, and $\sim 10\%$ stay in the extracellular space. Half of the data points are within the boxes, 80% are within the whiskers. Solid and dashed lines represent the medians and means, respectively. Round dots mark the maximum and minimum values. Diamond dots represent the raw data points. Statistics are from images taken from 45 regions of 3 different cultures. **b**, Confocal microscope time series images (upper middle, lower left, and lower middle; green, calcium; blue, Si nanowires) show that a glial cell with an internalized nanowire can be optically stimulated to trigger intracellular calcium elevation and subsequent intercellular calcium wave propagations to both glial cells and neurons. A differential interference contrast (DIC) image (upper left) highlights the nanowire under stimulation (black arrow) and the morphologies of a neighboring glial cell (red arrow) and a neuron (blue arrow). The laser illumination (592 nm, ~ 14.4 mW) was on for 1 ms right before the time point of 2.830 s. Quantitative analysis of the fluorescence intensities over time (right) from three regions of interest show calcium dynamics in all cells (black, the glial cell being stimulated; red, a nearby glial cell; blue, a neighboring neuron). **c**, Si nanowires can serve as a dual-role

intracellular biophysical tool, *i.e.*, a calcium modulator and a marker for motor protein-microtubule interactions. The location of a nanowire (*i.e.*, a transport marker) in a glial protrusion is tracked while the nearby calcium dynamics is monitored simultaneously, following a remote laser illumination of a different nanowire (*i.e.*, a calcium modulator) to initiate a calcium flux within the network (green, calcium; blue, Si nanowires; first one from left). The white dashed box marks the region of interest for the transport study. Time series images (second one from left, middle one, second one from right) show a calcium-correlated motion of the Si nanowire. MSD analysis further suggests a mode shift of the nanowire motion from random or restricted diffusions (rolling MSD diffusivity exponent, $\alpha \approx 1$) to an active transport ($\alpha \approx 2$). **d**, Microtubule networks can be mechanically manipulated by laser illumination (592 nm, 1 ms, ~ 2.09 mW) of intracellular Si nanowires. Red, microtubules; blue, Si nanowires. The white star marks the illumination site on the nanowire. **e**, Intercellular conduits can also be manipulated (592 nm, 1 ms, ~ 2.55 mW). Red, microtubules; blue, Si nanowires. A kymograph (lower right) taken along the white dashed line (upper left) shows the evolution of the conduit length. The white star marks the illumination site on the nanowire.

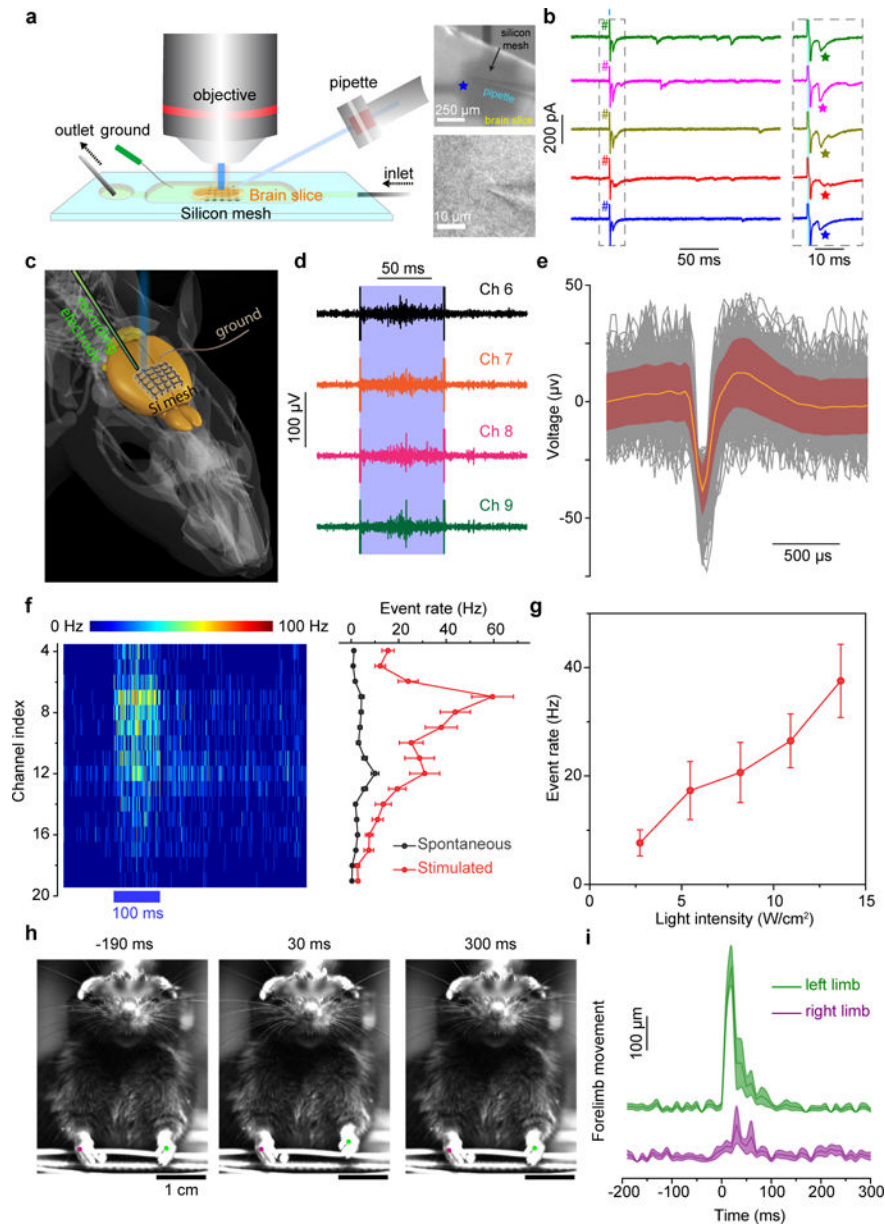


Figure 4 | Flexible and distributed silicon mesh for optically-controlled extracellular neuromodulation.

a, A schematic diagram of a photostimulation of a brain slice performed in a perfusion chamber (left). A pyramidal neuron in a cortex slice was held at -70 mV in the whole-cell voltage-clamp mode (lower right) while a distributed Si mesh was placed underneath the slice (upper right). Short laser pulses (473 nm, 1 ms, ~ 2 mW, ~ 57 μm spot size) were delivered to a spot on the Si mesh (marked by a blue star) to activate the nearby cells. **b**, Example traces from voltage clamp recordings of the patched pyramidal neuron over 5 trials (left) with 1-ms long laser stimulations (cyan bar). The grey dashed box marks the time frame for zoom-in views on the right. EPSCs are marked by stars following the illuminations of the Si mesh (right). The cyan shaded area marks the illumination period in each trial. # denotes the photoelectric artifact. **c**, A schematic diagram illustrating the *in vivo*

photostimulation test. A linear probe with 32 recording sites is guided into a head-fixed anesthetized mouse brain to sample the evoked neural activities by the illumination of an adjacent silicon mesh. **d**, Example traces of raw neural response data from four adjacent channels (Ch 6 to Ch 9) in a single trial of stimulation (473 nm, 100 ms, ~ 5 mW, ~216 μ m spot size) marked by a light blue band. **e**, A mean neuron-firing waveform (orange) superposed on individual waveforms (black) of both spontaneous and stimulation-evoked activities. The maroon shaded area denotes standard deviations. Data are from 300 waveforms, with 153 from stimulated events and 147 from spontaneous events, in one representative photostimulation experiment on one mouse. **f**, A heat map of PSTH for channels between 4 and 19 (left) and the mean spontaneous and evoked neural response rates across all trials for the same channels in the PSTH heat map (right). The blue bar underneath the heat map indicates the period of laser stimulation. Error bars denote standard error of the mean (s.e.m.) of the data from 50 trials in one representative photostimulation experiment on one mouse. **g**, The evoked mean neural response rate is positively correlated with the stimulation laser intensity. Error bars represent s.e.m. from 50 trials in channel 9 in one representative photostimulation experiment on one mouse. **h**, Snapshots of a forelimb movement study following photostimulations. The mouse's left limb (green dot) moves up and down following the laser illumination (473 nm, 50 ms, ~ 4 mW, ~ 216 μ m spot size) on a Si mesh attached to the right side of the forelimb primary motor cortex. See Supplementary Video 1 for more details. **i**, Time-dependent mean limb movements show a preferred motion of the left forelimb after the stimulation. The 0 ms time point represents the start of the light pulse. Shaded areas denote s.e.m. of the data. Data are from 15 trials in one representative photostimulation experiment on one mouse.

Table 1 |
A summary of individual photo-responses from 16 selected Si structures.

A *p-i-n* diode junction promotes the capacitive current (Red) over a uniformly doped *p*-type Si. Metal decorations on the *p-i-n* membrane surface further enhance the capacitive current (Red), and more importantly, increase the proportion of Faradaic component (Green). Laser illumination on Si materials with smaller dimensions yields stronger photothermal responses (Blue). The LED illumination condition: ~ 12.05 mW, ~ 500 μm spot size, ~ 6 W/cm²; the laser illumination condition: ~ 47.1 mW, ~ 5 μm spot size, ~ 240 kW/cm². Pipette-Si distance ~ 2 μm.

Light source	Si material	Capacitive (pA)	Faradaic (pA)	Thermal (K)
LED 530 nm 6 W/cm ²	p-type	49.8	14.6	0.0
	p-i-n	7388.4	6.5	0.0
	0.01mM	9525.4	45.2	0.1
	0.1mM HAuCl ₄	93305.0	1038.7	0.0
	1mM	95273.2	2184.4	0.0
	0.01mM	6193.1	89.5	0.0
	0.1mM K ₂ PtCl ₆	11784.0	242.9	0.0
	1mM	10935.0	93.1	0.0
	0.01mM	6887.7	30.3	0.1
	0.1mM AgNO ₃	10531.9	193.4	0.0
	1mM	6505.4	81.7	0.0
	Laser 532 nm 240 kW/cm ²	p-i-n bulk	4378.4	26.0
p-i-n 500 μm		484.8	0.7	0.6
p-i-n 100 μm		65.5	2.6	1.1
p-i-n 20 μm		30.0	6.9	2.8
i-i nanowire		14.3	1.9	5.4